Project Title:	Scattering Solar Thermal Concentrators
Project Period:	08/01/12 – 12/31/14
Project Budget:	$199,390
Submission Date:	01/27/15
Recipient:	Penn State University
Address:	Office of Sponsored Programs 110 Technology Center University Park, PA 16802
Award Number:	DE-EE0005798
Project Team:	Penn State University
Contacts:	Chris Giebink Assistant Professor Phone: 814-865-2229 Fax: 814-863-5341 Email: ncg2@psu.edu

Executive Summary:

The goal of this project was to explore a scattering-based approach to concentrate sunlight with the aim of improving collector field reliability and of eliminating wind loading and gross mechanical movement through the use of a stationary collection optic. The approach is based on scattering sunlight from the focal point of a fixed collection optic into the confined modes of a sliding planar waveguide, where it is transported to stationary tubular heat transfer elements located at the edges.

Optical design for the first stage of solar concentration, which entails focusing sunlight within a plane over a wide range of incidence angles (>120 degree full field of view) at fixed tilt, led to the development of a new, folded-path collection optic that dramatically out-performs the current state-of-the-art in scattering concentration. Rigorous optical simulation and experimental testing of this collection optic have validated its performance.

In the course of this work, we also identified an opportunity for concentrating photovoltaics involving the use of high efficiency microcells made in collaboration with partners at the University of Illinois. This opportunity exploited the same collection optic design as used for the scattering solar thermal concentrator and was therefore pursued in parallel. This system was experimentally demonstrated to achieve >200x optical concentration with >70% optical efficiency over a full day by tracking with <1 cm of lateral movement at fixed latitude tilt.

The entire scattering concentrator waveguide optical system has been simulated, tested, and assembled at small scale to verify ray tracing models. These models were subsequently used to predict the full system optical performance at larger, deployment scale ranging up to >1 meter aperture width. Simulations at an aperture widths less than approximately 0.5 m with geometric gains ~100x predict an overall optical efficiency in the range 60-70% for angles up to 50 degrees from normal. However, the concentrator optical efficiency was found to decrease significantly with increasing aperture width beyond 0.5 m due to parasitic waveguide out-coupling loss and low-level absorption that become dominant at larger scale.

A heat transfer model was subsequently implemented to predict collector fluid heat gain and outlet temperature as a function of flow rate using the optical model as a flux input. It was found that the aperture width size limitation imposed by the optical efficiency characteristics of the waveguide limits the absolute optical power delivered to the heat transfer element per unit length. As compared to state-of-the-art parabolic trough CPV system aperture widths approaching 5 m, this limitation leads to an approximate factor of order of magnitude increase in heat transfer tube length to achieve the same heat transfer fluid outlet temperature.

The conclusion of this work is that scattering solar thermal concentration cannot be implemented at the scale and efficiency required to compete with the performance of current parabolic trough CSP systems. Applied within the alternate context of CPV, however, the results of this work have likely opened up a transformative new path that enables quasi-static, high efficiency CPV to be implemented on rooftops in the form factor of traditional fixed-panel photovoltaics.

Table of Contents

Background:

The concept of scattering concentration has within the past few years been the subject of investigation by several groups with a corresponding flurry of papers published since this project began.[1-4] In general, they follow a similar waveguide coupling approach, where light is focused via a lenslet array onto embedded scattering elements. Additionally, they have also conducted initial forays into self-adaptive scattering response mechanisms. These publications were dismaying at first since they disclosed the same basic approach pursued in this project, but were nevertheless useful in answering some of our initial questions and ultimately helped to accelerate our own progress.

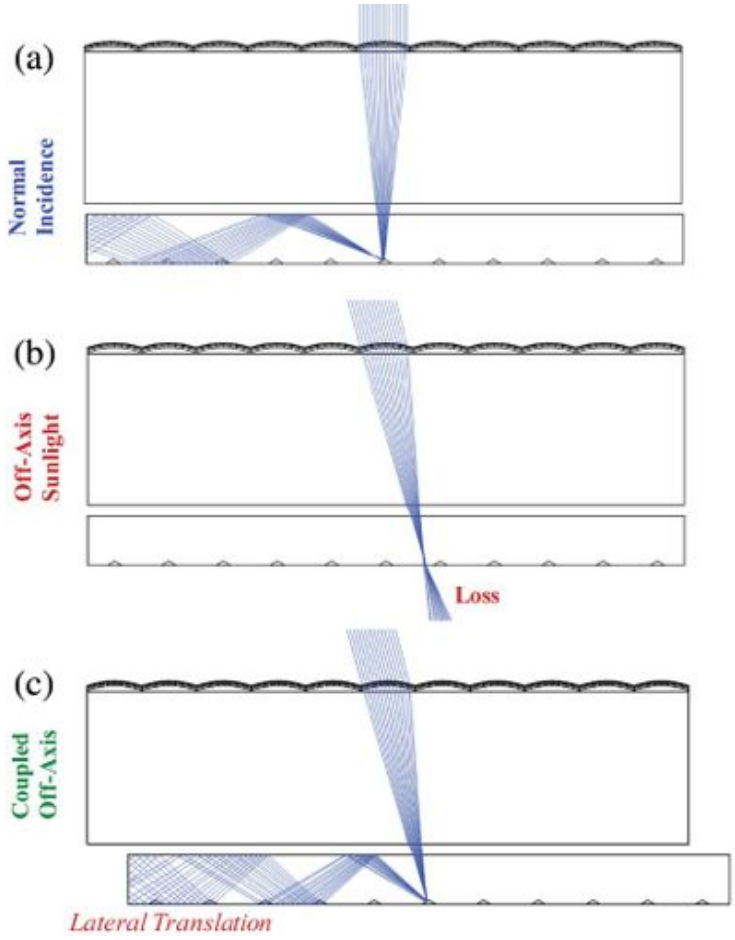

Figure 1. Lenslet array scattering concentrator explored in Ref. 1. Incident light is focused through a waveguide embedded with scattering elements that deflect it into confined modes, with tracking accomplished through lateral translation.

These publications implemented scattering concentration in a distributed fashion using a lenslet array as illustrated in Fig 1. Here, an upper lenslet array focuses light into a guide sheet that maintains a corresponding array of small, embedded scattering elements. Instead of moving the scattering element over the sheet as in our original proposal, the entire sheet itself is translated laterally. This work simulated and

experimentally tested a complete, 5 x 7 cm^2 prototype outdoors and achieved 65% optical efficiency at a geometric gain of 128x for an attached Si solar cell. The primary challenge identified for further improvement was off-angle performance due to the mismatch between scattering element position and the lens Petzval surface, which was subsequently solved through our work in Phase I.

The second important literature development explored the realization of self-adaptive scattering responses, which we also identified as an important opportunity in the supplement to our original proposal supplement last spring. As we discussed at that time, self-adaptive scattering, in which the high intensity focal point induces a local scattering response, constitutes the ultimate goal since it effectively enables high concentration with a completely passive system (at least from an outside control standpoint).

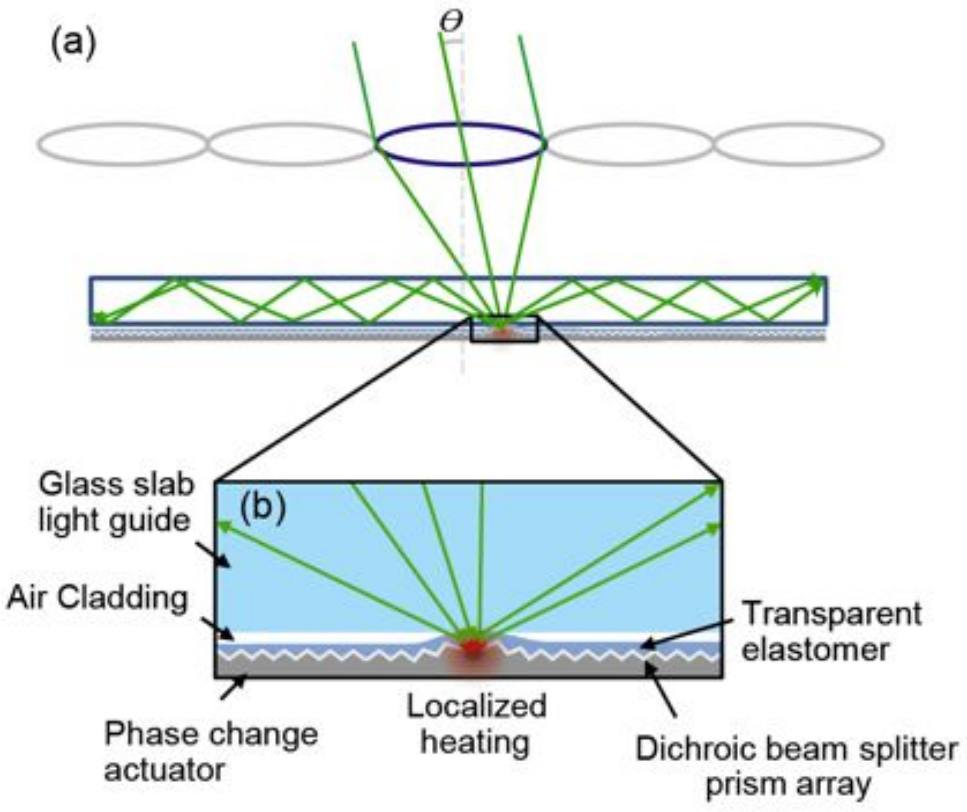

Figure 2. Self-adaptive scattering approach explored in Ref. 3, where localized heating at the focal point causes volume expansion, pushing the scatterer into conformal contact with the waveguide to enable local index-matched coupling into waveguide modes.

Several different approaches were published in the past two years based on thermally actuated local expansion, thermally-induced bubble formation and a refractive index change due to a dielectrophoretic response in a liquid light guide. The local thermal expansion approach shown in Fig. 2 used paraffin wax as the underlying phase change medium and achieved a weak, but clear self-adaptive coupling response.

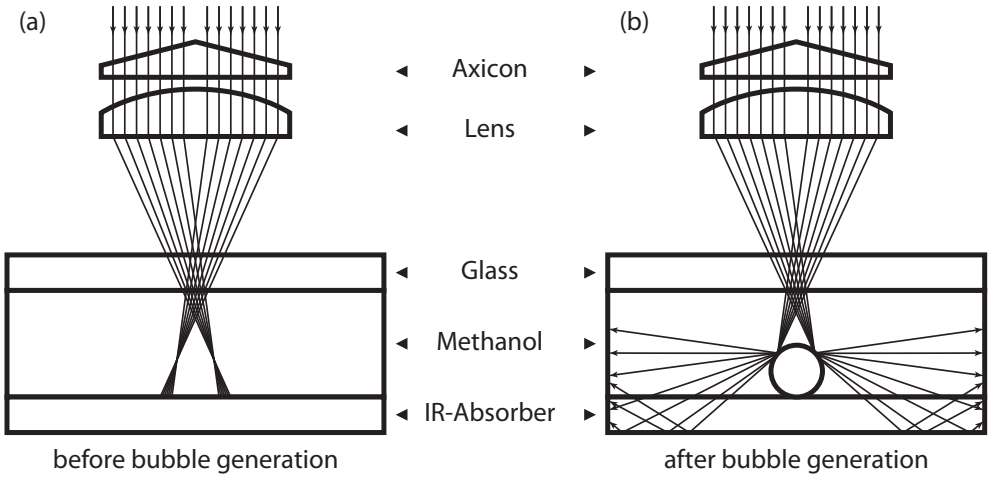

Figure 3. Schematic illustrating a local self-adaptive scattering response based on thermally-induced bubble formation described in Ref. 4.

Similarly, the bubble formation mechanism illustrated above in Fig. 3 also demonstrated a repeatable self-tracking capability, however, the response in all cases was very weak, with only a small fraction of the incident light coupled into the waveguide. These reports are important, however, because they demonstrate initial directions and proof of concept as well as the fact that several other groups have latched on to the same ideas that we are pursuing.

Introduction:

Solar tracking is the basis for all CSP systems, which rely on a large-area field of collectors that accounts for nearly half of the installed system cost. To date, the tracking requirement is met exclusively by moving large mirror surfaces to follow the diurnal and seasonal movement of the sun with high precision. This approach is both simple and effective, but it suffers from two principal drawbacks, namely, tracking error due to wind loading, and the high capital cost of the mirrors and support structure.

The scattering concentration approach pursued here was initiated with the goal of minimizing gross mechanical movement in the collector field as much as possible in order to mitigate wind loading and also to improve mechanical reliability of the tracking system. The advantages expected for a system with fixed collection optics are:

- Immunity from wind loading
- More efficient land use due to reduced shading
- Elimination of the need for spectrally selective HTE coatings
- More reliable operation due to decreased number of moving parts
- Lower capital and maintenance costs due to smaller tracking apparatus.

The metrics set out for this project build toward the lab-scale demonstration of a scattering concentrator with optical performance equivalent to existing, state-of-the-art parabolic trough designs, attaining peak and annual average optical efficiencies ≥75% and ≥55%, respectively, in conjunction with geometric concentration ratio >80.

Project Results and Discussion:

Collection optic design

The originally proposed collection optic involved an aspheric Fresnel lens together with a curved waveguide in order to follow the focal point over a wide angular range. The first task in the project was to identify an optical configuration to minimize the Petzval curvature. Such systems are well-known in the form of fish-eye wide-angle lens configurations, however, these are complicated involving many optics (= efficiency loss) and operate at a large F/# (=not compact). It was realized early in the project, however, that a bi-element refractive/reflective design represents a promising route to achieve a flat Petzval surface. As shown in Fig. 4 below, stacking a refractive top lens with a positive Petzval curvature on top of a reflective bottom lens with a negative Petzval curvature effectively enable cancellation leading to a nearly planar intermediate Petzval surface.

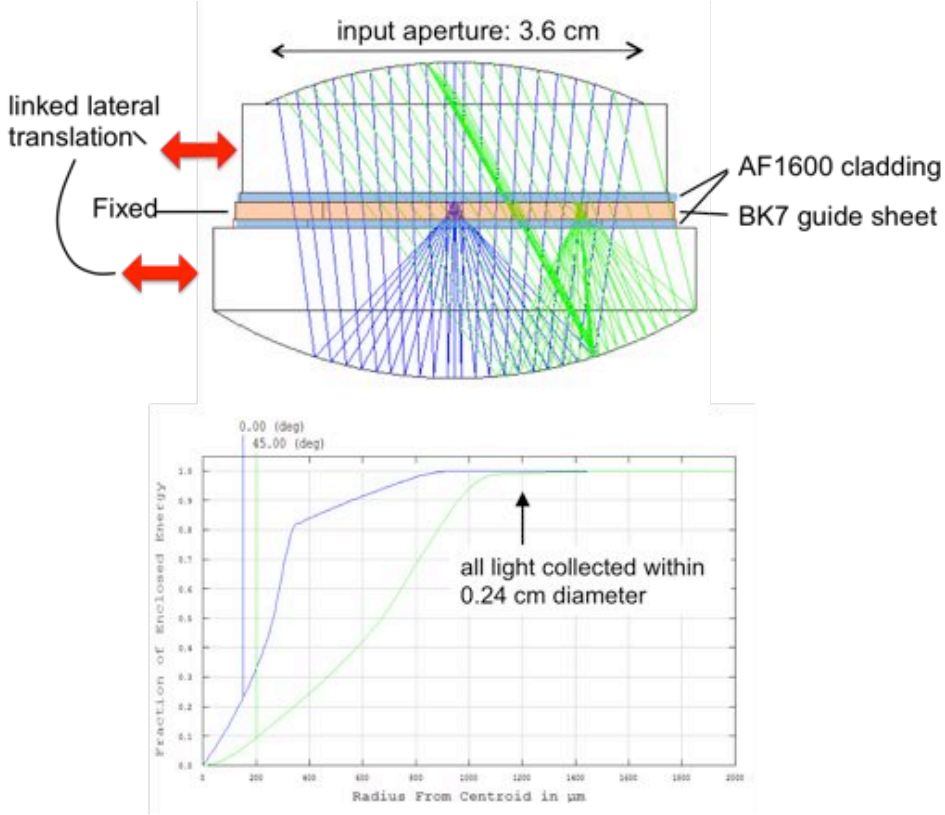

Figure 4. Ray-tracing illustration of the bi-element collection optic, where light is focused to the guide sheet located in the middle (shaded orange). The optics are made of acrylic and the guide sheet is BK7 glass layered on either side by PTFE cladding layers (shaded blue). The lower figure shows that all light is collected within a 2.4 mm diameter region in the guide sheet plane for both on (0°) and off (45°) axis light.

The resulting design is shown above in Fig. 4 and consists of the glass guide sheet sandwiched by an upper spherical refractive lens and a lower reflective mirror. The

lens/mirror combination is repeated laterally in the form of a lenslet-type array that is translated laterally over the fixed guide sheet which is embedded with a corresponding array of scattering elements. The guide sheet is clad with a thin coating of polytetrafluoroethylene (PTFE, e.g. Teflon) which has a low refractive index (n~1.3), high transmission across the solar spectrum, and a low coefficient of friction that enables the upper and lower optics to slide with ease.

This quasi-monolithic architecture offers several advantages in addition to enabling efficient wide angle focusing to a planar guide sheet:

1) It protects the guide sheet surface and prevents soiling, which was a concern in the original design with an exposed guide sheet.
2) It maintains the focusing optics at an exact, fixed distance relative to the guide sheet as they are translated, greatly simplifying the mechanics of tracking.
3) It improves transmission of incident light through the stack by lowering the refractive index contrast from air at the various interfaces.

Pursuant to the last advantage, we eliminate any potential air-gaps by utilizing a refractive index matching fluid that also serves as a lubricant to maintain ease in laterally translating the upper and lower optics. Because the lenslets are small (a few cm) and periodic, only lateral translation at a corresponding scale is necessary, reducing the task of tracking with a large collection optic to lateral translation less than a few cm in any given direction.

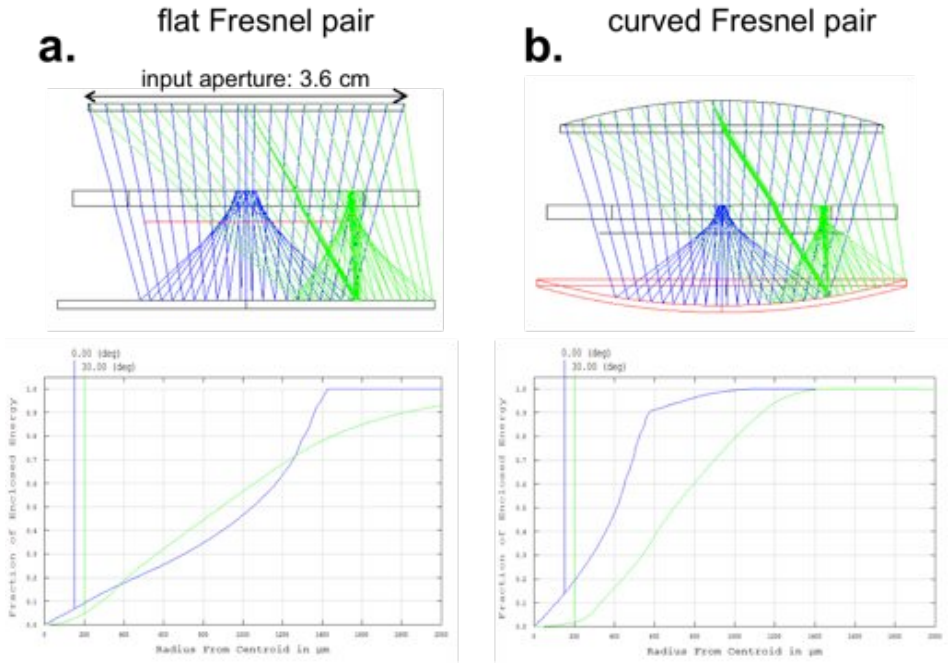

Figure 5. Optimization of (a) a flat Fresnel lens pair and (b) a curved Fresnel lens pair used to focus light to the guide sheet plane; the Fresnel lenses are made of acrylic plastic.

In addition to the lenslet approach, we also examined Fresnel-based extensions as shown in Fig. 5. In Fig. 5a, we optimized a refractive and reflective Fresnel lens pair to focus within the same guide sheet as in Fig. 4 using a nonlinear least-squares algorithm. Note that here the guide sheet is clad simply in air, though a PTFE coating could be added if needed both to protect the guide sheet from soiling and also to serve as an anti-reflection coating. The planar Fresnel lens performance is substantially worse than the lenslet element in Fig. 4, achieving a much lower off-angle efficiency at the same geometric gain according to their respective encircled energy diagrams at the focal spot. Curving the upper and lower Fresnel lenses as shown in Fig. 5b (i.e. independent Fresnel surface pitch and overall geometric curvature) and re-optimizing significantly improves the performance, nearly matching that of the lenslet system by achieving comparable off-axis performance.

We chose to focus our efforts on the lenslet approach because:

- it leads to the best overall collection optic performance and is compatible with inexpensive plastic optic components
- at only a few centimeters thickness, it is extremely compact
- it is essentially monolithic in that the only movement required is sliding of the different optics; there are no free standing components
- the required lateral translation is small, on the order of half the lenslet pitch which is on the order of centimeters.
- there is only a single optic surface (the upper lens surface) to clean; all other optic surfaces are internal to the structure and protected.

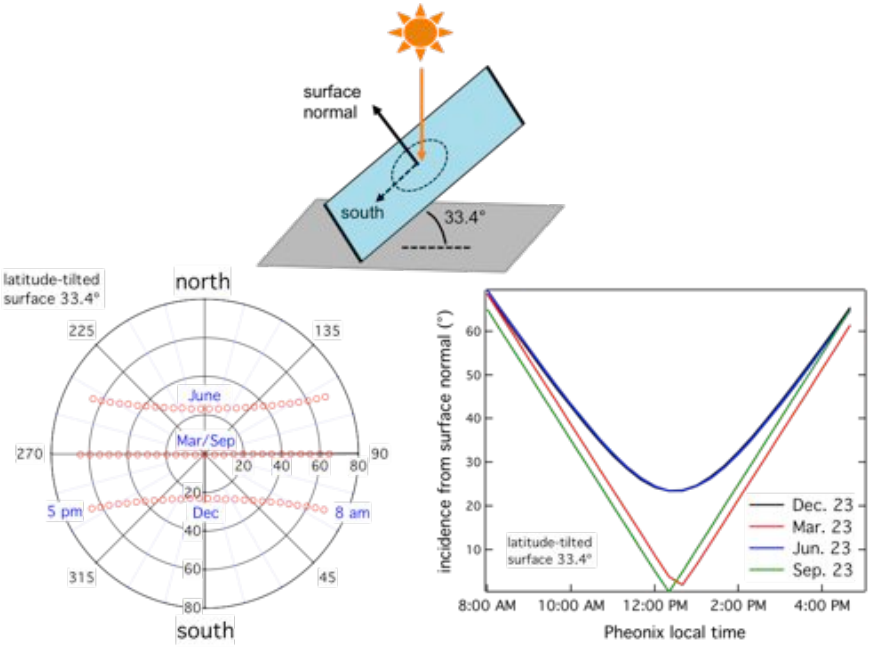

Figure 6. Solar path predicted using the NREL solar position algorithm, illustrating incidence angles expected for a latitude-tilted surface located in Phoenix, Az for different times of day.

Based on solar path calculations shown in Fig. 6, we also made a decision to place more stringent criteria on the range of incidence angles accepted by our collection optic, increasing the maximum acceptance range from ±45° to ±60°, which corresponds to an increase from ~6 to ~8 hours of operation per day.

To meet this challenge, we optimized our design using non-spherical lenslet surfaces via a nonlinear least squares algorithm and found that using hyperbolic curvature enables optimum performance as shown below in Fig. 7. There, >90% of the light in the focal plane falls within a spot size exceeding a geometric gain >280x at incidence angles up to 60°, which is a dramatic improvement upon the existing results of Ref. 1, where comparable performance was obtained only at angles <25°.

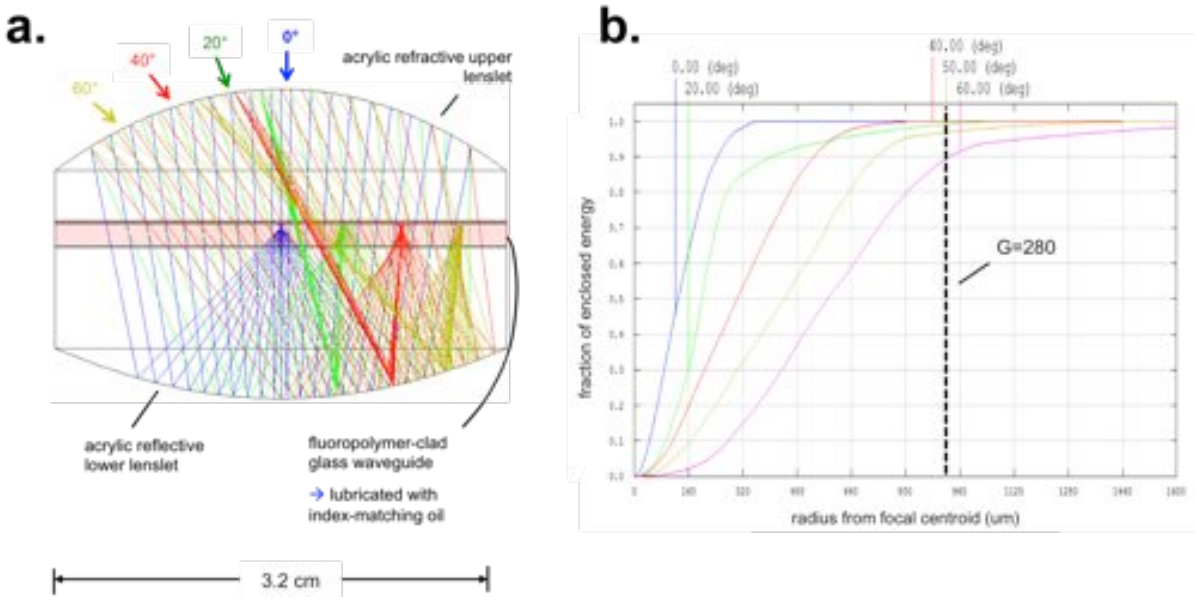

Figure 7. (a) Final optimization of the bi-element collection optic for incidence angles up to ±60°, where light is focused to the guide sheet located in the middle (shaded orange). The optics are made of acrylic and the guide sheet is 2 mm thick BK7 glass layered on either side by PTFE cladding layers lubricated with index matching oil. **(b)** Fraction of enclosed energy in the intermediate focal plane as a function of radial distance from the centroid.

After optimizing a single lenslet, we subsequently optimized an array with full non-sequential, polarization sensitive analysis as shown in Fig. 8 (see central shaded layout). The lenslet and thickness parameters are the same as in Fig. 1, except that the lenslets have a square aperture as defined by the array. Figures 8a and 8b depict a side view of the optical system, where the guide sheet is again BK7 glass shaded in orange and sandwiched by thin PTFE layers. The lenslet optics are made of acrylic and the lower reflective surface has a 100 nm evaporated Ag coating.

Figures 8c and 8d show the intensity distribution collected at the guide sheet focal plane for one of the lenslets for on-axis and 45° oblique illumination. Assuming randomly polarized, full spectrum sunlight, the on-axis optical efficiency was 85.6% and that for 45° incidence was 70.2%, collected within an area <2.4 x 2.4 mm^2 to maintain a

geometric gain of 225x. The optical efficiencies are lower than that for a single, circular lenslet due to corner loss arising from the square lenslet apertures.

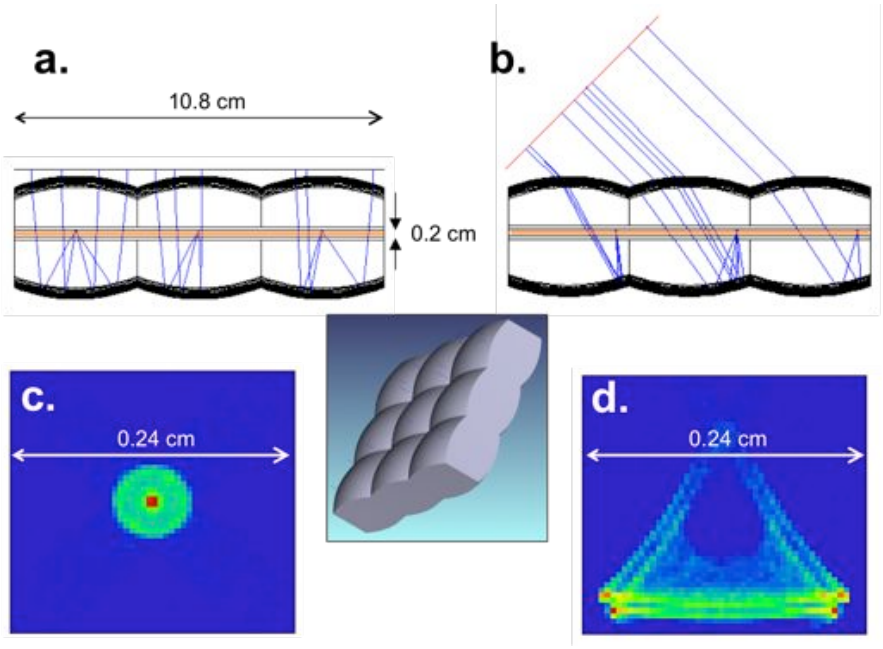

Figure 8. Full non-sequential analysis of a 9x9 bi-element lenslet array. Cases of normal incidence (a) and 45° off-axis illumination (b) are shown together with their respective intensity profiles in the guide sheet focal plane in (c) and (d) under a single lenslet. The guide sheet is shaded in orange and is sandwiched by PTFE cladding as in Fig. 7. The center graphic shows a rendering of the entire optic.

Increasing the array symmetry to hexagonal tiling reduces corner losses as expected and demonstrated in Fig. 9 below. There, the geometric gain was maintained at 225x, however, the optical efficiency improved off-axis at 45° to 75%, substantially better than its square array counterpart.

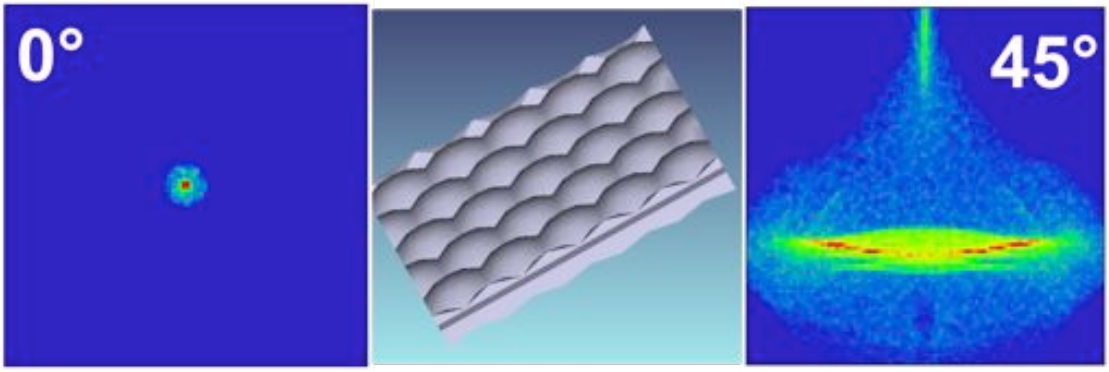

Figure 9. Simulations maintaining the same parameters and geometric gain as in Fig. 8, but using a hexagonal lens tiling to reduce corner losses and improve off-axis optical efficiency.

The performance of the hexagonal lenslet collection optic over the full 0-60° incidence angle range is shown below in Fig. 10. A range of azimuthal angles was also simulated for this optic and shown to vary only by ~2% due to the symmetry of the hexagonal tiling

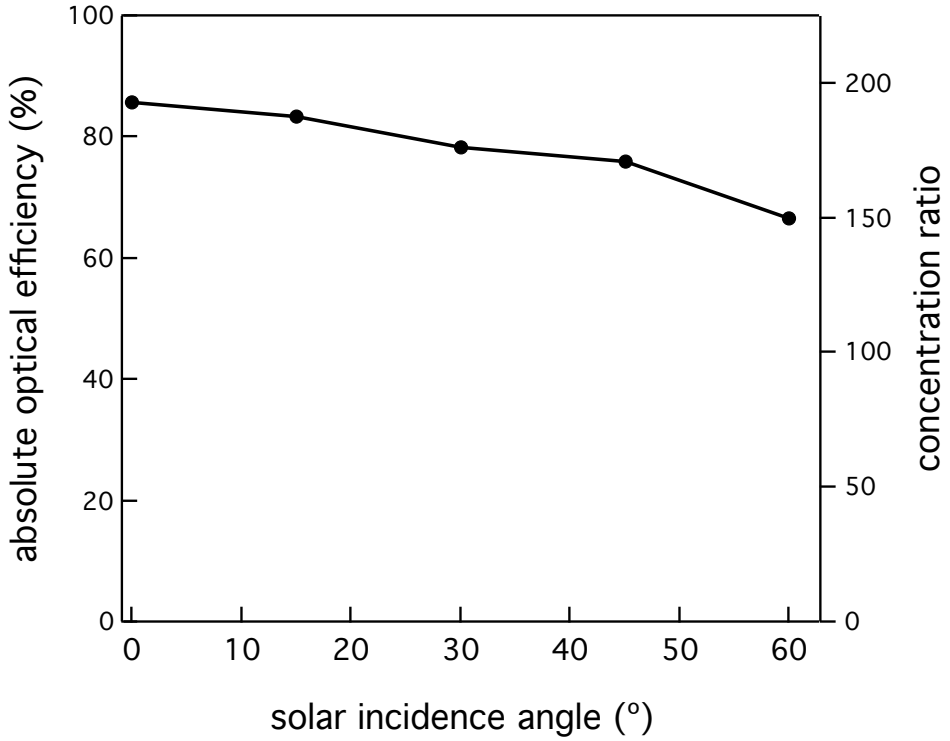

Figure 10. Absolute optical efficiency predicted as a function of solar incidence angle for the hexagonal lenslet collection optic shown in Fig. 9, fabricated from acrylic plastic.

In addition to optimization, we also analyzed the sensitivity of these designs to slope error in manufacture. Variation in conic constant of the lenses by up to 50% had little effect on the performance except at very wide angle (>50°). In fact, forgoing the optimized hyperboloidal curvature in favor of simple spherical curvature maintained >90% of the optimized optical efficiency, again for incidence angles <50°. This was shown also when experimentally testing with spherical commercial lenses, where surprisingly efficient operation was obtained. The bi-element design therefore appears to be fairly robust.

Scattering element design

We began by investigating both grating based scatterers as well as geometric specular scattering elements. Initial grating results were predicted using the rigorous coupled wave/Fourier modal method, however it rapidly became clear that we could not achieve the needed efficiency over a large enough spectral bandwidth to make this a viable option. Specular scatterers by contrast proved simple and efficient. We began by considering single reflective pyramidal and conical scatterers embedded in the guide sheet under the simple ray geometric constraint, $\theta_{wall} = \left(\theta_{\max} + \theta_{crit}\right)/2$, relating the scatterer wall angle to the critical angle of the guide and the maximum ray angle at the

focal point. It is therefore important to determine the range of incidence angles impinging at the focal point as a function of incidence angle on the concentrator. These angular distributions are shown in Figs. 11b and 11c for normal and wide angle (60°) solar incidence on a square lenslet, where the important conclusion is that focal point incidence angle remains confined within ~ ±45° irrespective of solar incidence angle. This does not change materially in the case of hexagonal tiling.

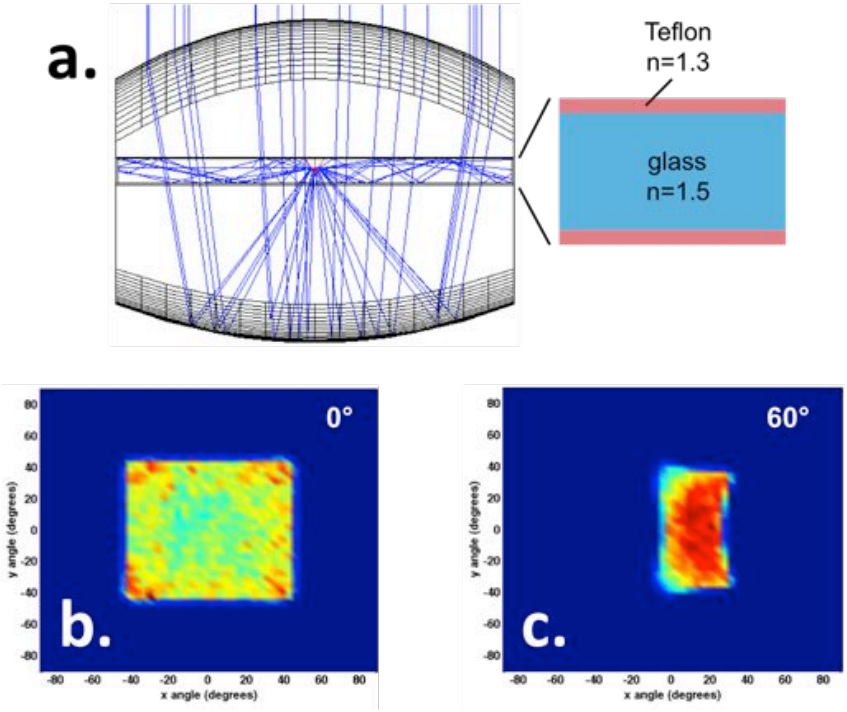

Figure 11. **(a)** Ray tracing schematic of a lenslet section and reflective conical scatterer embedded in the waveguide. **(b)** Range of incidence angles incident at the on the scattering element at normal incidence and at 60° incidence (c).

Taking for example, the conic scatterer, by properly choosing the conic size (base diameter ~2 mm) and wall angle (~52°) in accord with the above relationship, together with a silver reflective coating, we obtained in-coupling efficiencies (light incident at the focal point → light trapped within the waveguide) of 91% at normal incidence and 80% at 60° incidence. Very similar numbers were achieved for four-sided and three-sided pyramidal shapes with optimum wall angles. Simple, two-sided wedges were also investigated and found to give reasonable results, with 70-80% incoupling over the full range of solar incidence angles.

Despite their lower incoupling efficiency, the benefit of wedge-type scatterers is that scattering is favored in two in-plane directions instead of the isotropic in-plane pattern resulting from an e.g. conic scatterer. At a full system level, in-plane directivity

is desired in order to minimize propagation length enroute to the edge-mounted heat transfer elements.

We determined a rigorous optimum solution using nonimaging optical analysis. Viewed from this perspective, the problem is one of etendue transformation as depicted in Fig. 12a, where light at the focal area with the given range of incidence angles must be transformed into light propagating orthogonally within the waveguide thickness and output angles confined within the total internal reflection cone.

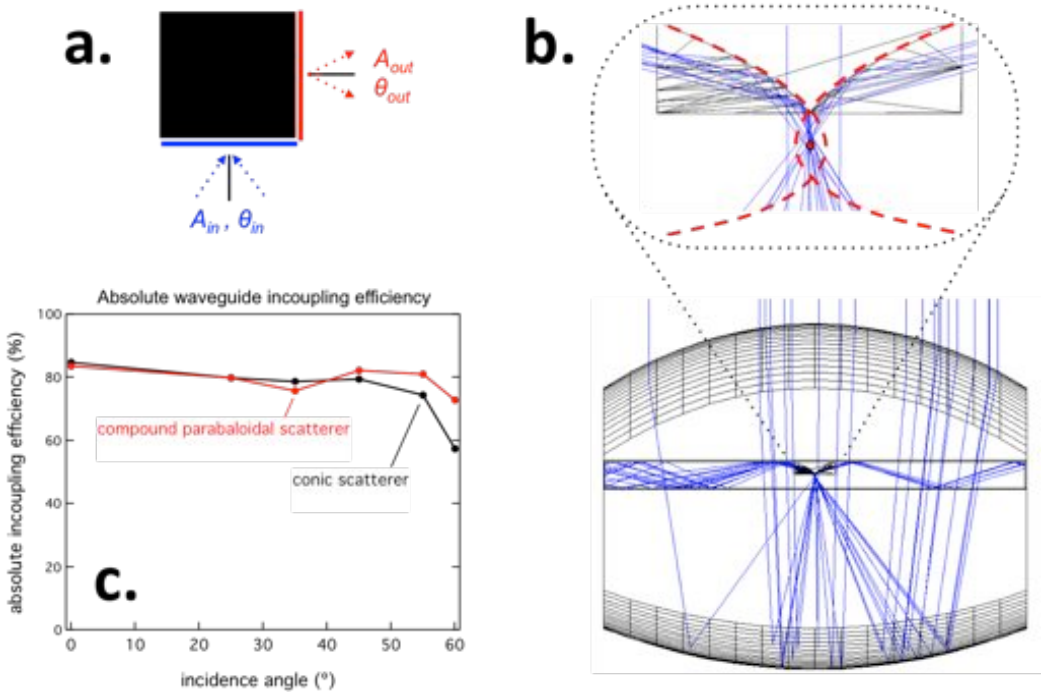

Figure 12. **(a)** Outline of the nonimaging etendue transformation problem of waveguide coupling. **(b)** Schematic of the compound parabaloidal scattering element solution, where rays passing through the collection optic focal point are redirected within the waveguide plane. **(c)** Absolute in-coupling efficiency for the compound parabloidal and conical scattering elements. Efficiency is defined as power coupled into the waveguide over that initially incident on the collection optic.

The solution to this problem is a compound parabaloidal optic shown in Fig. 12b. It consists of a curved, wedge-like reflector composed of two off-axis parabaloids whose foci are centered on the collection optic focal point. Rays crossing directly through the focal point are thereby redirected directly along the plane of the waveguide; rays not directly coinciding with the focal point remain at high angles, trapped by total internal reflection. Figure 12c shows the absolute waveguide in-coupling efficiency (i.e. the fraction of power incident on the concentrator that is coupled into confined waveguide modes) for both the conic and compound parabaloidal scatterers. Both show high in-coupling efficiency over a wide range of angles, however, the compound parabaloid is ultimately advantageous because it scatters primarily in two directions as opposed to the conic, which scatters equally in all directions.

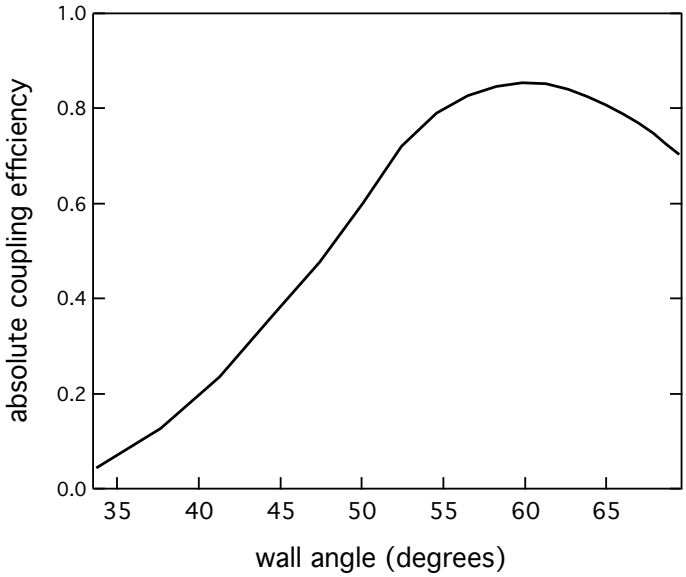

Figure 13: Incoupling efficiency of the conical scattering element as a function of wall angle (i.e. angle between the base and side of the cone).

We have also investigated potential manufacturing non-idealities through our simulations, including the effect of slope errors and non-specularity of the conical and compound parabaloidal features. Slope errors in the conical scatterer are manageable when kept below ± 5° of the optimum as shown in Fig. 13 above. The slope angle tolerance is similar for the compound parabaloid though this is more difficult to parameterize in a plot.

We have also theoretically evaluated the effect of non-specularity on the scattering element surface by applying a standard Gaussian scattering model where the

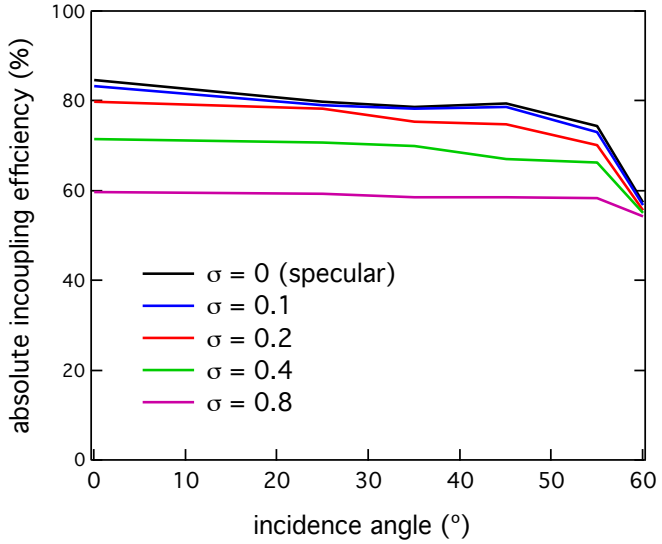

Figure 14: Incoupling efficiency for the conical scattering element as a function of Gaussian surface scattering half-width σ.

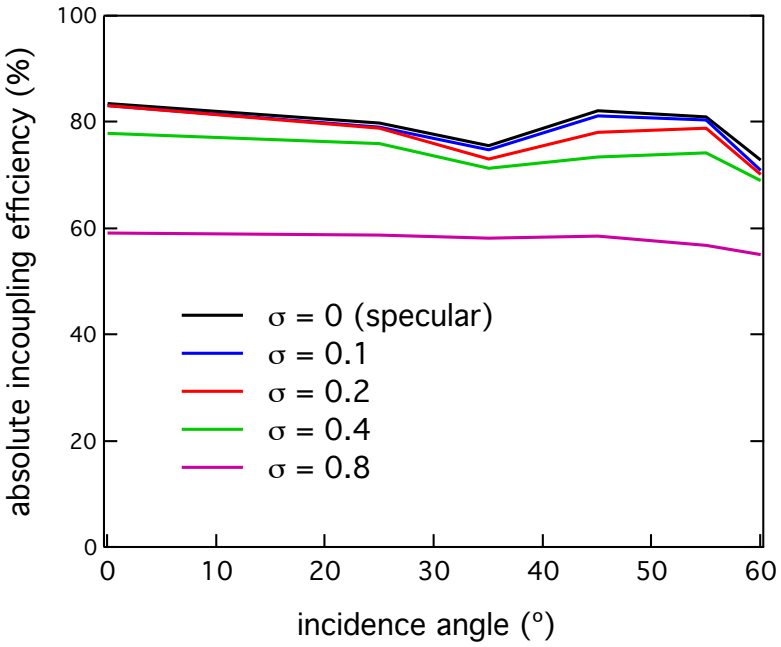

Figure 15: Incoupling efficiency for the parabaloidal scattering element as a function of Gaussian surface scattering half-width σ.

bidirectional scattering distribution function is proportional to $\exp\left[-|\vec{x}|^2/\sigma^2\right]$, where $\vec{x}$ is the in-plane unit scattering vector. The incoupling efficiency for the conical and compound parabaloidal elements is displayed below in Figs. 14 and 15 respectively, where σ is varied between 0.1-0.8 (limiting values of $\sigma \sim 5$ approach completely randomized Lambertian scattering). It is evident for both elements that a substantial drop in efficiency occurs for $\sigma > 0.2$. For reference, polished metal surfaces such as those being used for our scattering element fabrication and also in processes such as optics injection molding routinely achieve specularity with $\sigma < 0.1$.

Heat Transfer Element Design

To minimize convective and conductive heat transfer, the heat transfer element (HTE) is contained in an evacuated tube situated between two adjacent waveguide sheets. To simplify the simulation, the HTE was modeled as an ideal black body, such that any light impinging on its surface was absorbed. The first design employs direct end-fire coupling from a flat-edged sheet waveguide with an anti-reflection (AR) coating into an evacuated cavity enclosed by a silvered parabolic mirror (Fig. 16).

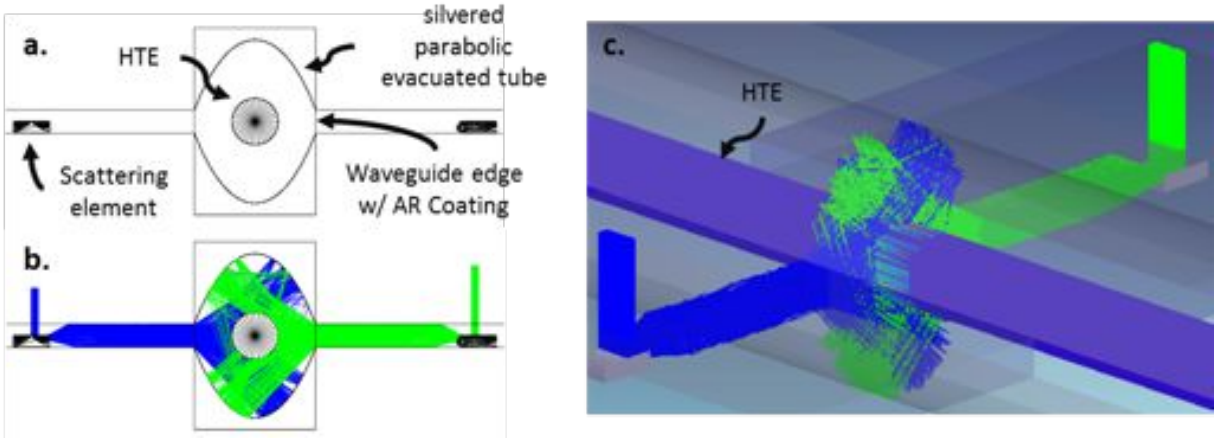

Figure 16. Different views of the flat-edge waveguide end-fire HTE coupling case. **(a)** A labeled section view of the flat-edge waveguide including ray trajectories traced in the simulation (b). **(c)** Three-dimensional shaded view of the simulation showing the relative intensity distribution on the HTE.

This simulation predicts that light trapped in the guide sheet exits into the HTE cavity with an efficiency of 97.4%. In the HTE cavity (i.e. the evacuated region between the silvered parabolic mirrors), there is a 43/57 percent split between light directly incident on the HTE and light that hits the walls of the cavity and is then reflected back onto the HTE. The only optical losses from this design come from reflection at the waveguide-vacuum interface and reflection losses from the silvered parabolic surface; a negligible fraction of light scatters out of the chamber once it has entered, giving this design an overall optical coupling efficiency of 95.1%.

Illumination uniformity on the central blackbody HTE element is evident in Fig. 16c, which shows red streaks at the top of the HTE and a number of blue areas denoting a higher and lower flux recorded at these locations, respectively. We found that the illumination homogeneity could be further increased by incorporating a concave flare into the waveguide edge to increase the fraction of light transmitted directly to the HTE as shown in Fig. 17, which constitutes a substantial improvement relative to that of conventional focusing parabolic trough collectors.

Because guided light propagates through the sheet with a distribution of angles determined by the scattering element, a small fraction of the light is reflected at the curved surface of the sheet edge. To compensate for this, the waveguide protrudes slightly into the chamber to capture as much of this back-scattered light as possible; the drawback to this strategy is that it increases the chance that rays scattered within the HTE chamber can exit back into one of the waveguides. These two loss mechanisms add up to a 1.7% loss in efficiency from the flat-edged waveguide, giving this design a lower optical coupling efficiency of 93.6%. A full thermal analysis will have to be performed to determine whether the loss in efficiency and increased manufacturing complexity of the flared edge are compensated by the more even flux distribution on the surface of the HTE.

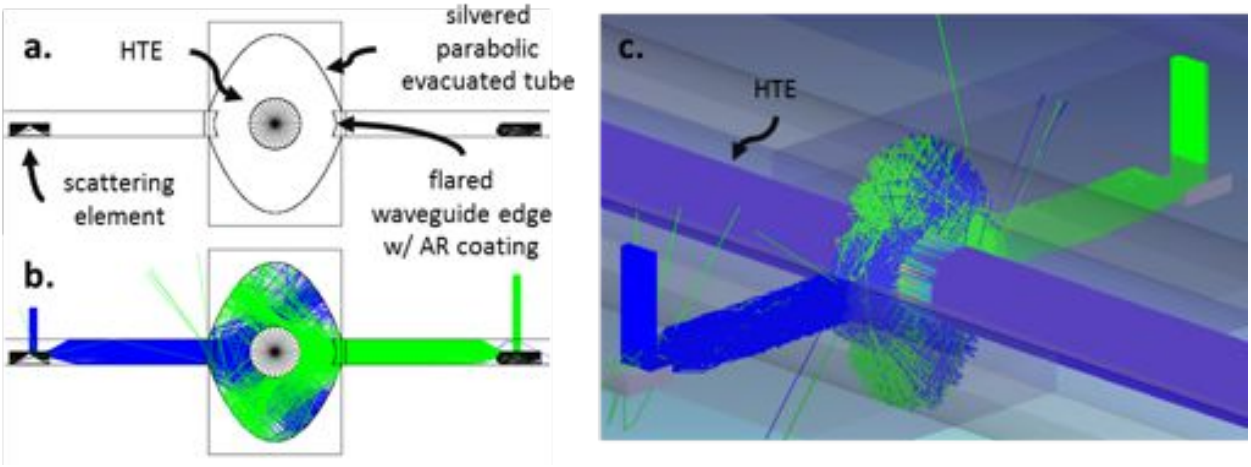

Figure 17. Different views of the flared-edge waveguide. **(a)** A labeled section view of flared-edge waveguide along with that including ray trajectories shown in (b). **(c)** Shaded view of the flared-edge waveguide showing the relative intensity distribution on the HTE.

Table 1. Summary of results for outcoupling designs.

	Light Exiting the Waveguide (%)	**Outcoupling Efficiency to HTE (%)**	**Light Directly Incident onto the HTE (%)**	**Light Reflected onto the HTE from the Cavity (%)**
Flat Edge Waveguide	97.4	95.3	43.1	56.9
Concave Edge Waveguide	96.1	93.6	46.0	54.0

Table 1 provides a summary of metrics for the two designs, as discussed above. Fig. 18a shows the relative difference in the amount of light that is transmitted from the waveguide to the HTE cavity as well as a comparison of the final outcoupling efficiency, and Fig. 18b presents a breakdown of the path that light takes in reaching the HTE (e.g. direct from the waveguide facet or reflected from the silvered parabolic enclosure).

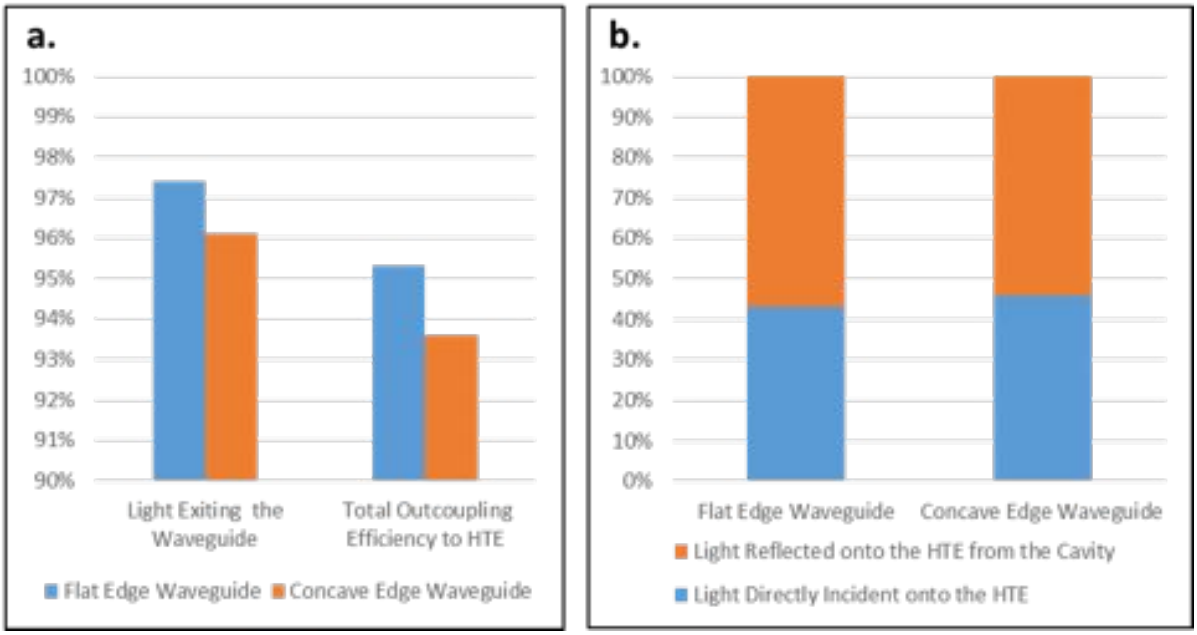

Figure 18. Graphical summary of results. **(a)** Comparison of light extracted from the waveguide and outcoupling efficiency to the HTE. **(b)** Breakdown the path taken by light from the waveguide to the HTE.

The overall complexity involved in constructing and maintaining an endfire coupling strategy such as this in the field is a concern. A potential solution to this issue could involve monolithic sheet waveguides with integrated scattering elements and HTE evacuated cylinders manufactured in single, integrated units as shown in Fig. 19. In this case, loss of efficiency resulting from a misalignment of the waveguide to the evacuated cavity containing the HTE could be reduced and ease-of-assembly for the end user increased. In this scenario, the only remaining components required to fabricate a planar solar-thermal concentrator would be the linear positioning system and complementary arrays of refractive/reflective lenslets, which would be assembled on site.

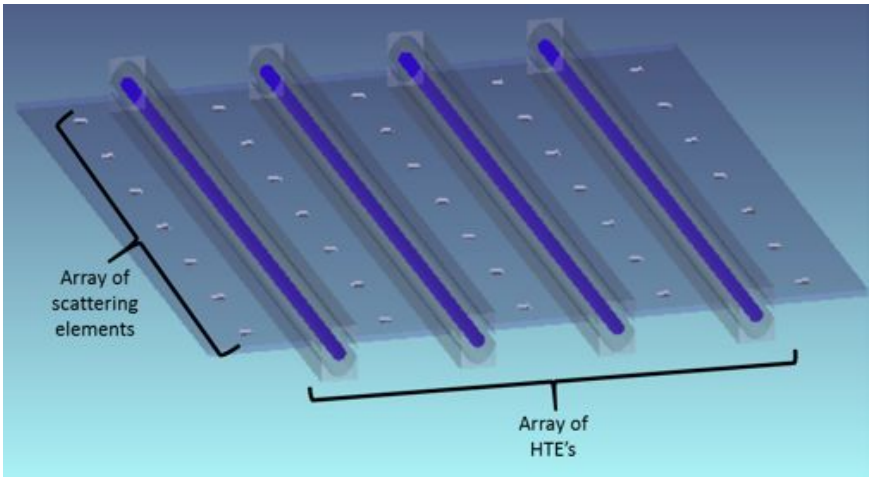

Figure 19. Monolithic array of scattering elements and HTEs

Full System Optical Simulation

Coupling the results of the collection optic and scattering element subsystems, we simulated the performance of a complete scattering concentrator system and began the process of global optimization. Figure 20 below shows a complete hexagonally-tiled concentrator, 0.448 m wide (e.g. separation between HTEs) at a geometric gain of 112x with 3.2 cm acrylic lenslet optics sandwiching a 2 mm thick BK7 glass guide sheet. Figure 20b predicts an overall optical efficiency >60% for incidence angles up to 55° for the compound parabaloidal scatterer, with lower high angle efficiencies for the conic scatterer. Here, optical efficiency is defined as the ratio of power exiting the two HTE edges relative to that incident on the concentrator and geometric gain, $G = L/2t$, where *L* is the concentrator width and *t* is the guide sheet thickness.

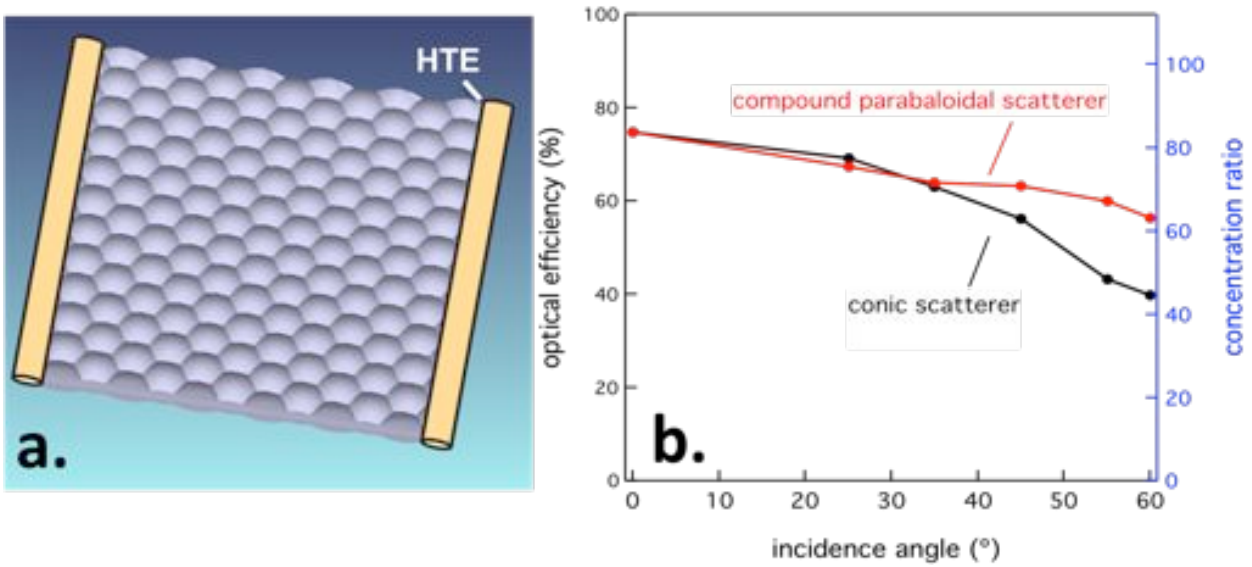

Figure 20. **(a)** Schematic of a complete lenslet-based scattering concentrator, simulated at solar incidence angles ranging from 0-60°. **(b)** Optical efficiency for a 0.448 m wide concentrator with geometric gain 112x. Efficiency is defined as power delivered to the two linear heat transfer elements located at the waveguide edges over that incident on the concentrator.

We have also examined scaling relationships and interactions among the various design parameters. Increasing the concentrator width and waveguide thickness proportionally, the performance scales directly as expected (e.g. doubling all dimensions maintains a constant geometric gain and optical efficiency) for widths less than about 0.5 m. Approaching this length, the optical efficiency begins to drop significantly due to increasing relevance of absorption in the glass guide sheet parasitic outcoupling loss by the scattering elements. Increasing geometric gain by widening the concentrator at fixed waveguide thickness also negatively impacts the optical efficiency since additional propagation distance within the guide sheet increases the likelihood of parasitic out-coupling by another scattering element.

In the optimization process, many factors were varied, including the concentrator aperture size, lenslet size, waveguide thickness, scattering element rotation, uni- and bidirectional compound parabolic scatterers, and tiling pattern. Key parameters are illustrated in Fig. 21a and Fig. 21b and include the aperture width (*d*; distance between heat transfer elements), the lenslet tiling pattern (square vs. hexagonal) and lattice constant (a_0), and the local scattering element rotation angle (θ).

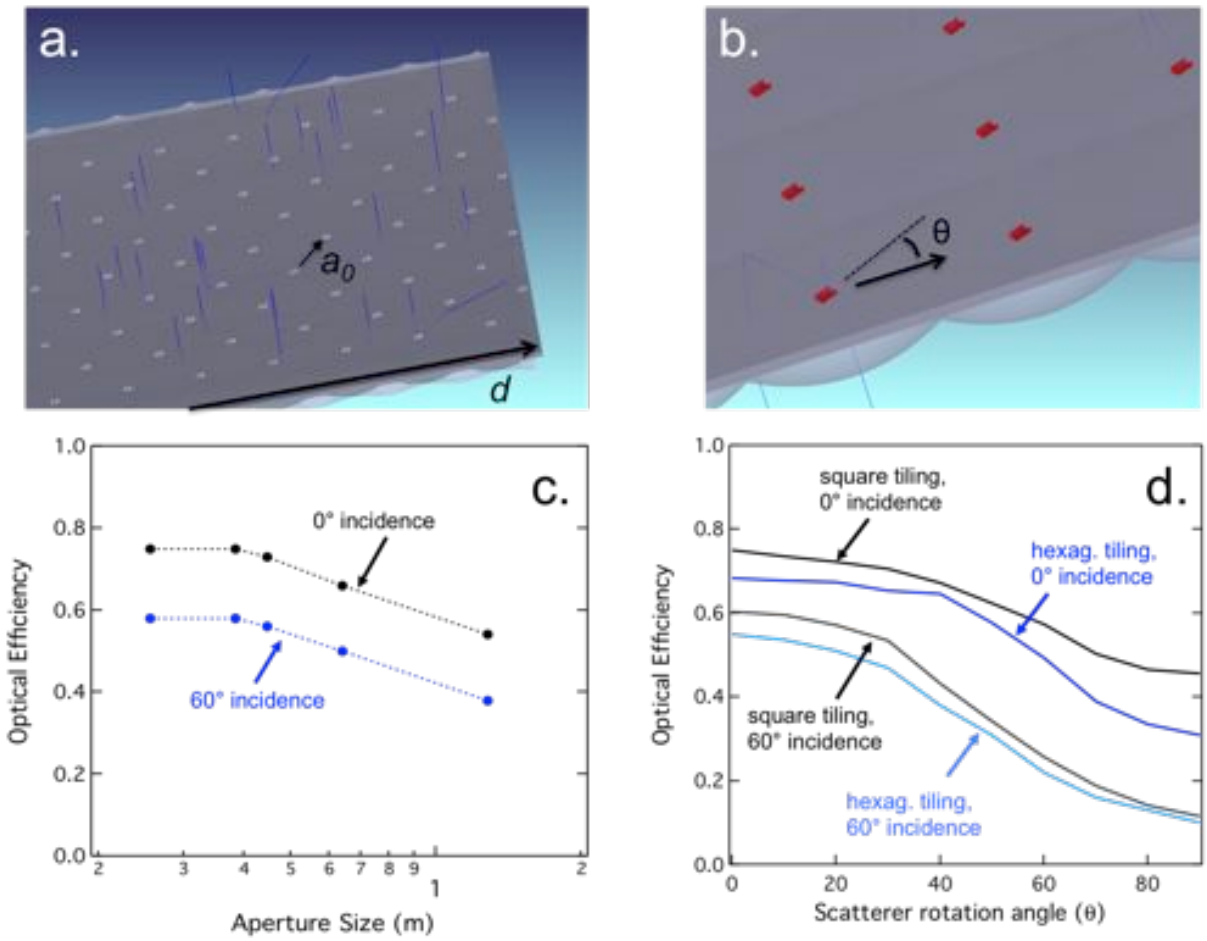

Figure 21. (a) Illustration of a section of scattering concentrator showing the aperture width, tiling geometry, and lattice constant. The top lenslet array has been made transparent for clarity. **(b)** Illustration showing local scattering element rotation angle, where zero degrees corresponds to orientation directly toward the heat transfer element edges. **(c)** Zemax simulation results for a square tiled array with 3.2 cm lattice constant as a function of aperture size. **(d)** Simulated optical efficiency for square and hexagonally-tiled arrays as a function of scatterer rotation angle.

Starting with square tiling at a 3.2 cm lattice constant and varying the aperture width at 0° and 60° incidence in Fig. 21c, we observe that the optical efficiency is largely constant at small sizes but begins to decrease substantially for d > 0.5 m at both normal and oblique incidence angles. This decrease is due to the combination of increasingly important glass absorption and parasitic waveguide decoupling from additional scattering elements. Figure 21d examines the impact of square vs. hexagonal lenslet

tiling with variation of the local scatter rotation to identify whether an appropriate combination can reduce parasitic outcoupling loss. Once might expect that slight rotations in the scatterer orientation could decrease decoupling by increasing the dominant path length between scatterers however it is clear from the data that this is not the case, with orientations at 0° (i.e. scattering directly toward the edges) most effective for both tiling geometries at all incidence angles.

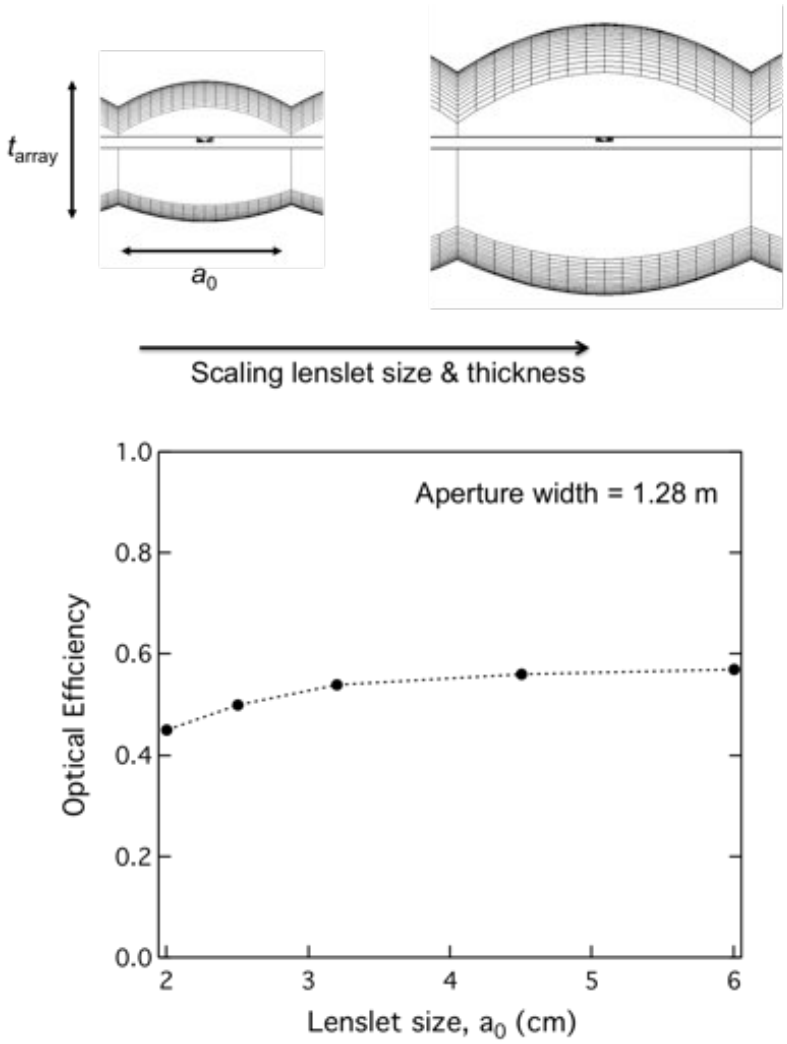

Figure 22. The upper panel illustrates the manner in which lenslet lattice constant / size scales for a constant waveguide thickness and aperture width. Increasing lenslet lattice constant decreases the overall number of scattering elements in the waveguide. The lower panel displays simulated optical efficiency as a function of lattice constant, demonstrating a significant dependence only for lenslet size falling well below 3 cm.

Lenslet size relative to the aperture width, which determines the number of lenslets in the array is another variable of interest. Increasing lenslet size decreases the number of scattering element in the waveguide and therefore reduces parasitic decoupling loss. This scaling is illustrated in the upper portion of Fig. 22, where the waveguide thickness and overall aperture width are maintained but the lenslet lattice constant is increased.

Simulations bear out expectation: as the lenslet size decreases below 3.2 cm, the optical efficiency begins to drop as the number of scattering elements becomes substantial and decoupling becomes dominant of intrinsic glass absorption. Importantly however, increasing the lenslet lattice constant carries diminishing returns while significantly increasing the thickness of the array and therefore overall material utilization (i.e. acrylic) and cost, rationalizing the a_0 = 3.2 cm optimum.

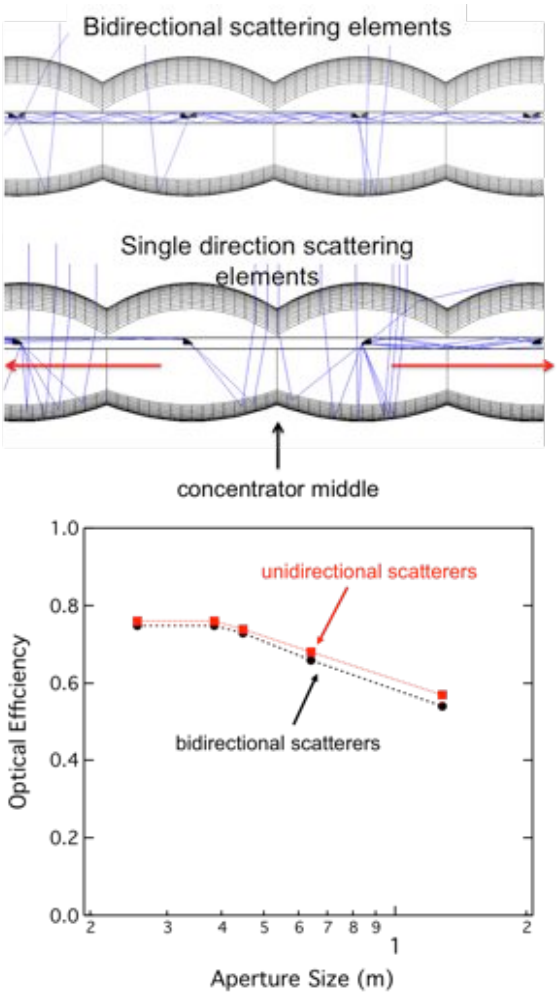

Figure 23. Illustration of bidirectional and unidirectional parabolic scattering elements. In the bidirectional case, light received on the left hand side of the waveguide that is scattered to the right must traverse the entire aperture width whereas unidirectional scatterers decrease the maximum propagation path lengths by approximately a factor of two. This results is a marginal improvement in optical efficiency at larger aperture width as indicated the simulation.

A natural approach for reducing parasitic decoupling is to exploit unidirectional rather than bidirectional scattering elements as illustrated in the upper portion of Fig. 23. By dividing the scattering element array at the middle of the concentrator into element facing in opposite direction, the average optical path within the waveguide decreases since light is not required to propagate the entire aperture width. The simulation result for implementing this strategy in a square array as a function of aperture size indicates

a negligible benefit at small sizes where parasitic decoupling is insignificant and become relatively more beneficial at larger aperture width. The benefit of decrease path length from unidirectional scatterers is somewhat tempered by the larger size required for them (i.e. a larger decoupling cross section for waveguided light).

Implementing the intuition gained from these and other simulations, targeted optimization using the Zemax Hammer optimization scheme and multiple variables (lenslet size, aperture size, scatterer rotation, waveguide thickness) for square and hexagonally-tiled arrays were carried out. The results follow the intuitive conclusions described above, yielding optima for square tiling with lenslet lattice constant of ~3 cm and ~0.5 m aperture width with zero degree scatterer rotation.

Concentrator Fabrication and Testing

Scattering element fabrication is conducted by controllably imprinting a metal mold into sections of an acrylic plastic sheet. Although the guide sheet ultimately would be made from glass instead of plastic, it is much more practical at this experimental stage to test using imprinted acrylic due to lower cost and faster turn around time.

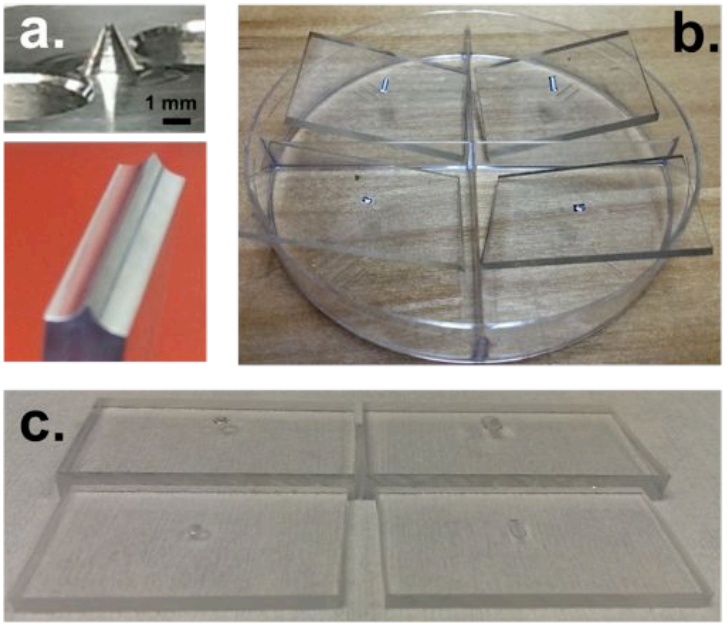

Figure 24. **(a)** Pictures of typical conic and compound parabaloidal scattering element imprint molds machined from aluminum. Scattering elements imprinted in acrylic sheets are shown in (c) and again in (b) after coating with 100 nm of Ag.

Figure 24 below shows two of the aluminum imprint molds used in the imprinting process, including a conical point and a compound parabaloidal wedge. Imprinted sheets of acrylic are shown in Figs. 24b and 24c after and before coating with a 100 nm Ag reflective layer, respectively. Optical profilometry images were attempted to asses the surface quality, however, insufficient signal was returned from the sloped surfaces and so we are continuing to explore methods for characterizing surface quality.

To test the in-coupling performance of these elements, we constructed a solar illumination and scattering efficiency test setup shown in Fig. 25a. The setup consists of a laser-driven Xe lamp source (LDLS), which produces a broad spectrum (190nm to >2um) from an extremely small plasma (100 um diameter), providing us with highly collimated (parallelism <0.5°) output light when coupled out with a series of parabaloidal mirrors. The beam can be redirected to a monochromator as shown below to obtain monochromatic light for measuring the spectral response of a scatterer; it also duals for testing collection optic performance as detailed in the following section.

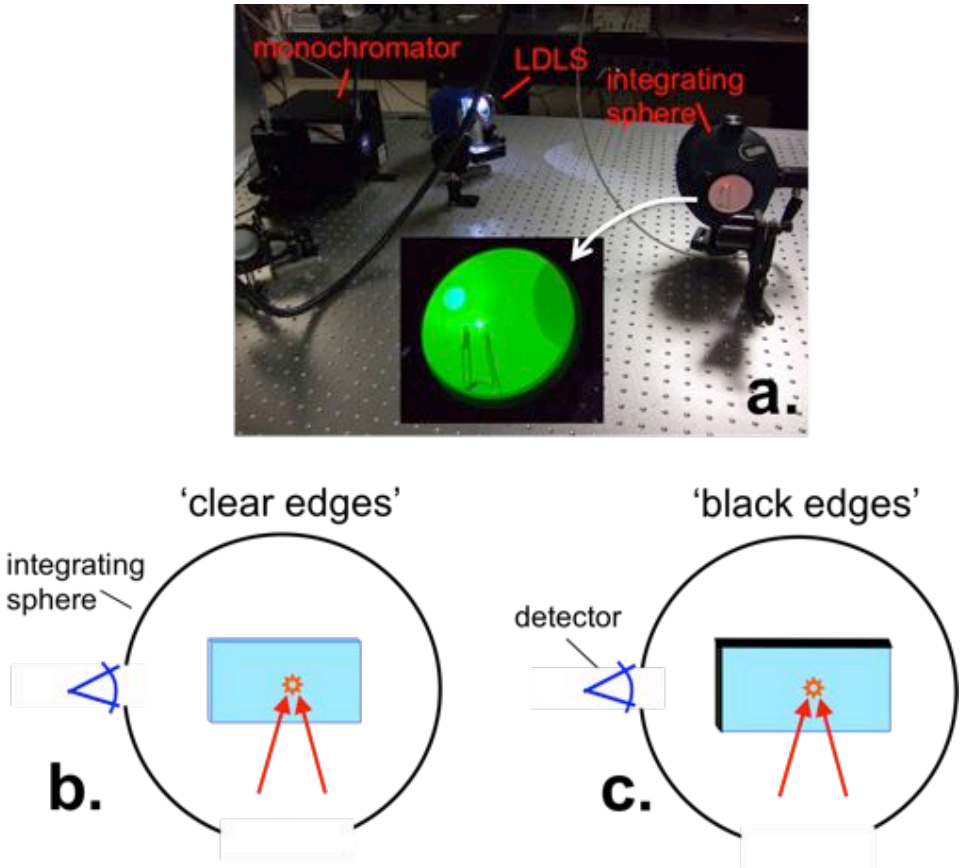

Figure 25. **(a)** Scattering efficiency and solar illumination testing setup. The inset shows the glass sample inside the integrating sphere with monochromatic green light focused on the sample inside the sphere. **(b)** Light is focused onto a small waveguide section with a scattering element at the focal point, re-directly light into the waveguide. In **(c)**, the edges are blackened with ink to eliminate signal due to guided light; the difference between configurations b and c is the light in-coupled into the waveguide.

Figures 25b and 25c outline our method for testing the scatterer-guide sheet coupling efficiency using an integrating sphere. The glass sample is first situated inside the integrating sphere and light from the monochromator is focused on the element and detected by a baffled detector at the side of the sphere. The sample edges are

subsequently blackened and the same measurement is then repeated, sweeping over wavelengths from 400-1100 nm. When the edges are blackened, this eliminates the contribution of light guided out the glass edges and thus the difference of these measurements provides the amount of light coupled into the glass according to $\eta_{scatt} = \left(I_{clear} - I_{black}\right)/I_{clear}$, where I_{clear} and I_{black} are the intensities measured in the sphere for clear and blackened edge samples, respectively (see Fig. 25).

Typical scattering results obtained for both conical and parabaloidal scatterers are shown below in Fig. 26.

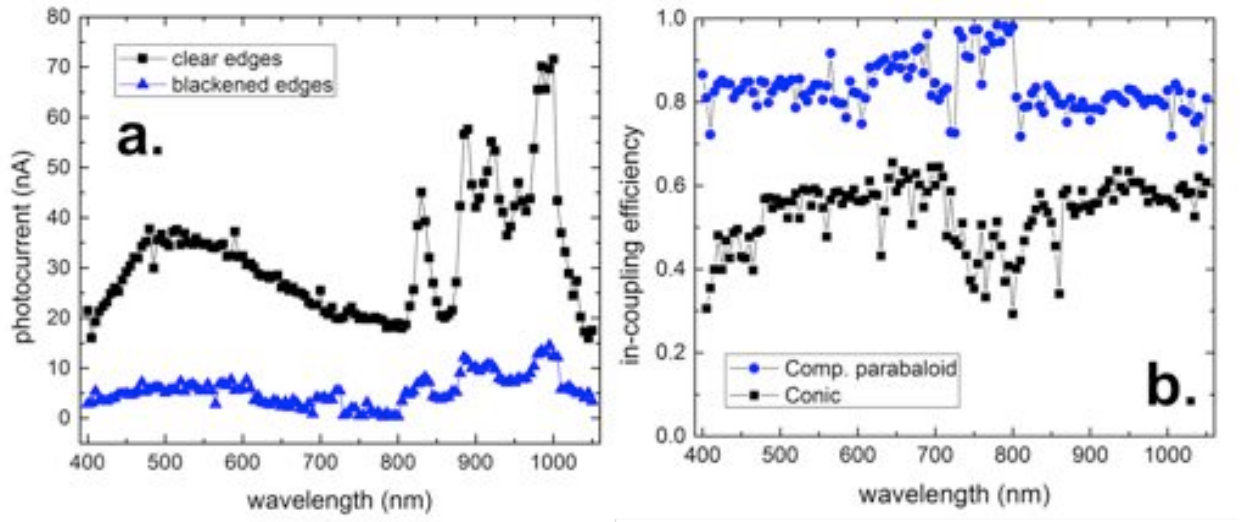

Figure 26. **(a)** Scattering spectra measured in the integrating sphere for a compound parabaloidal element with clear and blackened edges. **(b)** Scattering efficiency measured for typical compound parabaloidal and conical scattering elements.

Figure 26a shows typical scattering spectra measured in the integrating sphere for a compound parabaloidal element with clear and blackened (with tape) edges. The difference in these two intensities represents the light trapped within the acrylic waveguide. The resultant in-coupling efficiency, η_{scatt}, is plotted in Fig. 26b for a conical and compound parabaloidal scattering element.

Beyond our efforts to design and test fixed scatterers, a small component of our work early on also focused on exploring approaches to realize self-adaptive scattering. In particular, we examined the possibility of using a buckling instability between two films with differing thermal expansion coefficient in order to temporarily create wrinkles that cause scattering. This process is well-studied in the common elastomer polydimethylsiloxane (PDMS) when coated with thin metal films. Thermally-induced wrinkling in metal-coated PDMS films produces isotropic wrinkling features with lateral length scale and amplitude on the ~10 micron scale.[5] In addition, because the Fourier transform of the wrinkle pattern is largely isotropic,[6] it was expected that the scattering might be reasonably efficient (20-40%) and therefore worth exploring.

We fabricated thermally-wrinkled PDMS films in our thermal evaporator and then tested their in-coupling efficiency using our integrating sphere setup. Typical scattering spectra are shown in Fig. 27a for a PDMS wrinkled sample, however, there is only a small difference between the clear and blackened edge case, resulting in only a 7-12% scatter coupling efficiency. We tried varying the thickness of the metal over-layer along with that of the PDMS film, which changes the reflectivity as well as the characteristic wrinkling length, however, we were unable to increase the incoupling efficiency above 30% averaged over the spectrum.

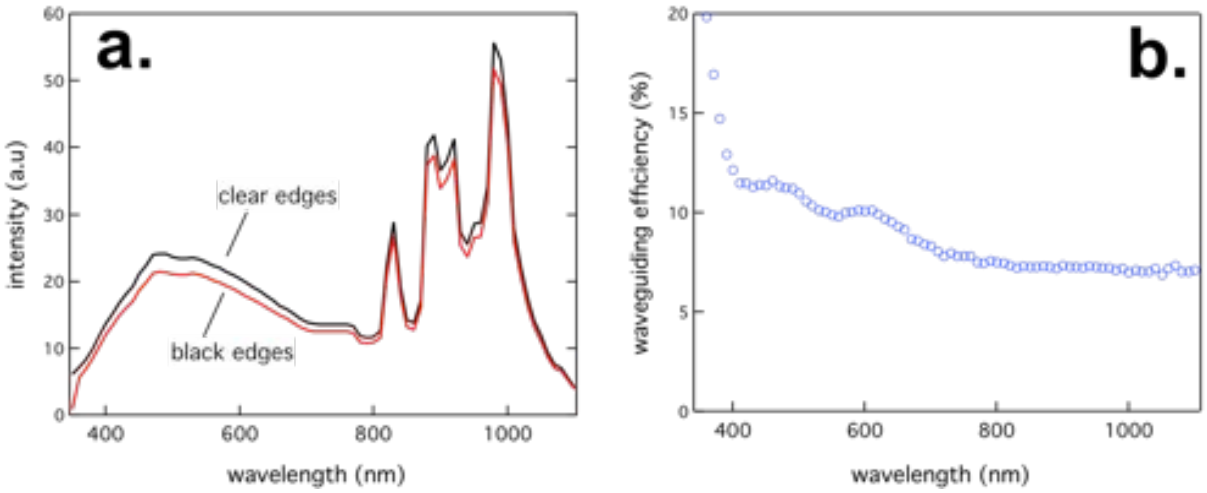

Figure 27. (a) Scattering spectra measured for an Al-metallized, wrinked PDMS film coated on glass, which results in the waveguide coupling efficiency calculated in **(b)**.

This level is substantially below that required in our design and, together with the difficulty of implementing this approach in our bi-element collection optic, lead us to discard this approach and focus entirely on translation mechanical microtracking.

Collection Optic Testing

Our collection optic design was tested initially using off-the-shelf commercially available lenses in conjunction with microcell photovoltaics supplied by collaborators at the University of Illinois. Off-the-shelf, 12.7 mm diameter BK7 commercial lenses were used to construct the bi-element collection optic design, with a reflective Ag coating deposited by thermal evaporation. The microcells were transfer-printed onto custom thickness glass and the complete optic was assembled with Norland optical adhesive and index matching fluid. Figure 28 illustrates the assembly of the collection optic together with images of the 700 x 700 μm transfer-printed microcell.

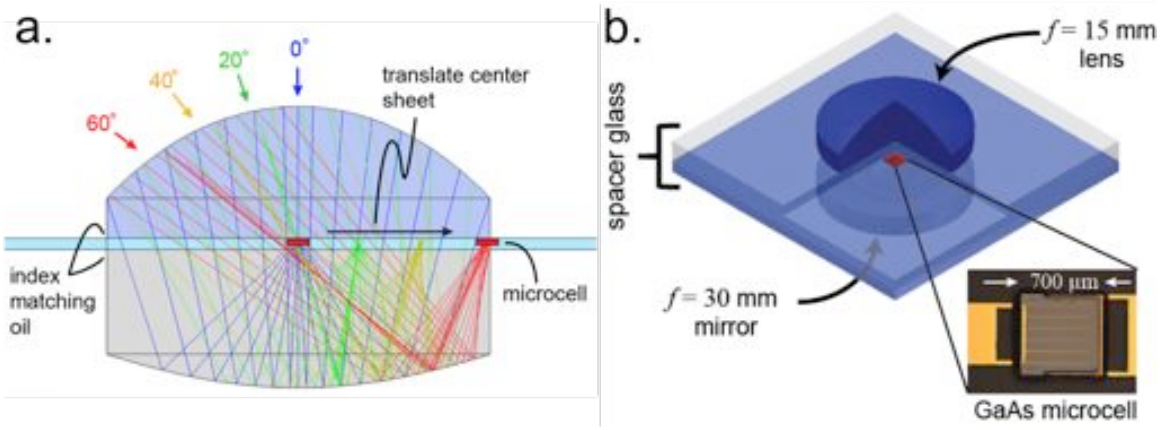

Figure 28. (a) Ray-tracing schematic illustrating the folded-path in a single-element collection optic and the translation-based microtracking approach operating over a wide range of angles. **(b)** The single element collection optic implemented with two commercial planoconvex spherical lenses and a GaAs microcell photovoltaic shown in the inset.

A picture of the test setup is shown below in Fig. 29, involving the same lamp source used in the scattering element testing above. Light is delivered from above and the entire collection optic apparatus slides along a track to test varying incidence angles from 0-70°. Tracking is accomplished manually via the pair of crossed translation stages evident in the photograph. The translation stages are adjusted for each incidence angle to maximize the short-circuit current of the PV cell, which is then referenced to the current obtained without concentrating optics. The short-circuit current is linearly related to the incident power and this has been verified up to the highest light intensities reached in the course of our experiments.

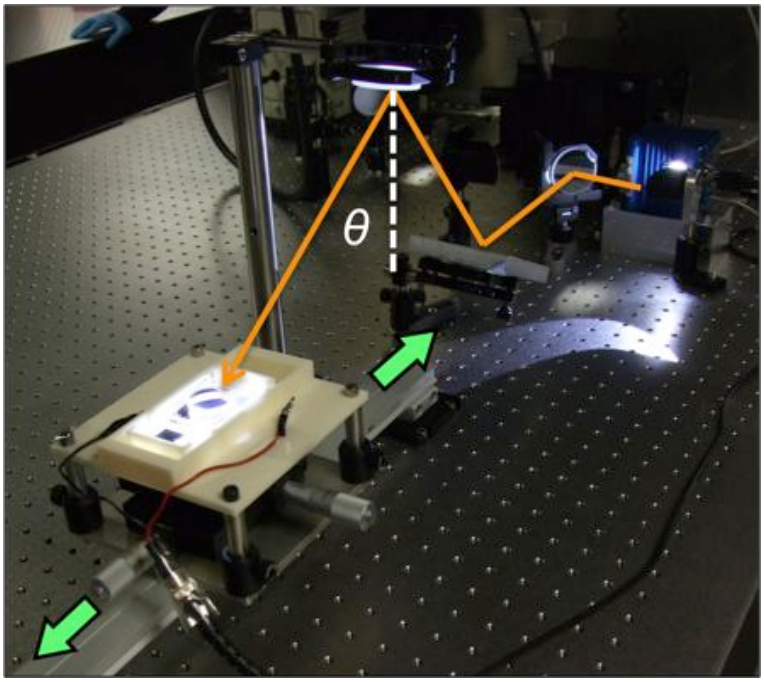

Figure 29. Photograph of the experimental setup for testing collection optics.

The results are shown in Figure 30a, which presents the short-circuit current measured for the bare microcell ($\boldsymbol{J_0}$) together with that integrated in the concentrator stack ($\boldsymbol{J_{CR}}$) as a function of incidence angle. Since the photocurrent is directly proportional to absorbed optical power, the difference marks a roughly constant 210-fold increase in the average intensity delivered to the microcell (i.e. $\boldsymbol{CR \approx 210}$) for incidence angles ranging up to $\boldsymbol{\theta_{inc} = 55°}$ that is reproduced in simulation as shown in Figure 30b. As indicated by the red dashed line, this increase is nearly equivalent to that obtained at normal incidence using the bare microcell and a plastic Fresnel lens with the same geometric gain ($\boldsymbol{G = 260}$).

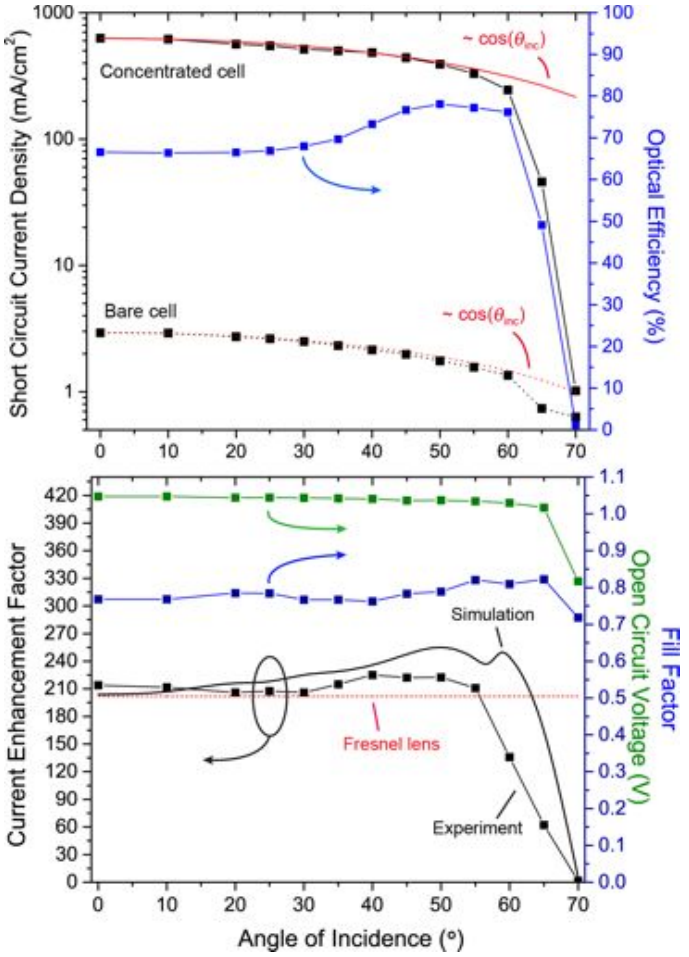

Figure 30. (a) Short-circuit current measured from the microcell in and out of the concentrator as a function of incidence angle. In both cases, the current dependence is largely described by the geometric cosine projection loss, indicating a nearly constant optical efficiency as shown on the right-hand axis. **(b)** Effective concentration ratio plotted as a function of incidence angle together with the fill factor and open-circuit voltage. Good qualitative agreement is observed with Zemax simulation indicated by the solid black line.

Because the photocurrent angle dependence in each case follows the cosine projection intensity loss designated by the red dashed lines in Figure 30a, the optical efficiency of

the concentrator itself is largely independent of incidence angle. It is estimated on the right-hand axis of Figure 8b according to $\boldsymbol{\eta_{opt}} \approx \boldsymbol{J}_{CR}\boldsymbol{T}_{ac}/\boldsymbol{GJ_0}\langle \boldsymbol{T}_{cc}\rangle = \boldsymbol{0.71}$, where $\boldsymbol{T}_{ac}(\boldsymbol{\theta})$ is the spectrally-averaged Fresnel transmittance from air into the microcell and $\langle \boldsymbol{T}_{cc}\rangle$ is that from glass into the microcell averaged over the range of angles, $\boldsymbol{\theta_{rec}}$, in Figure 6a.

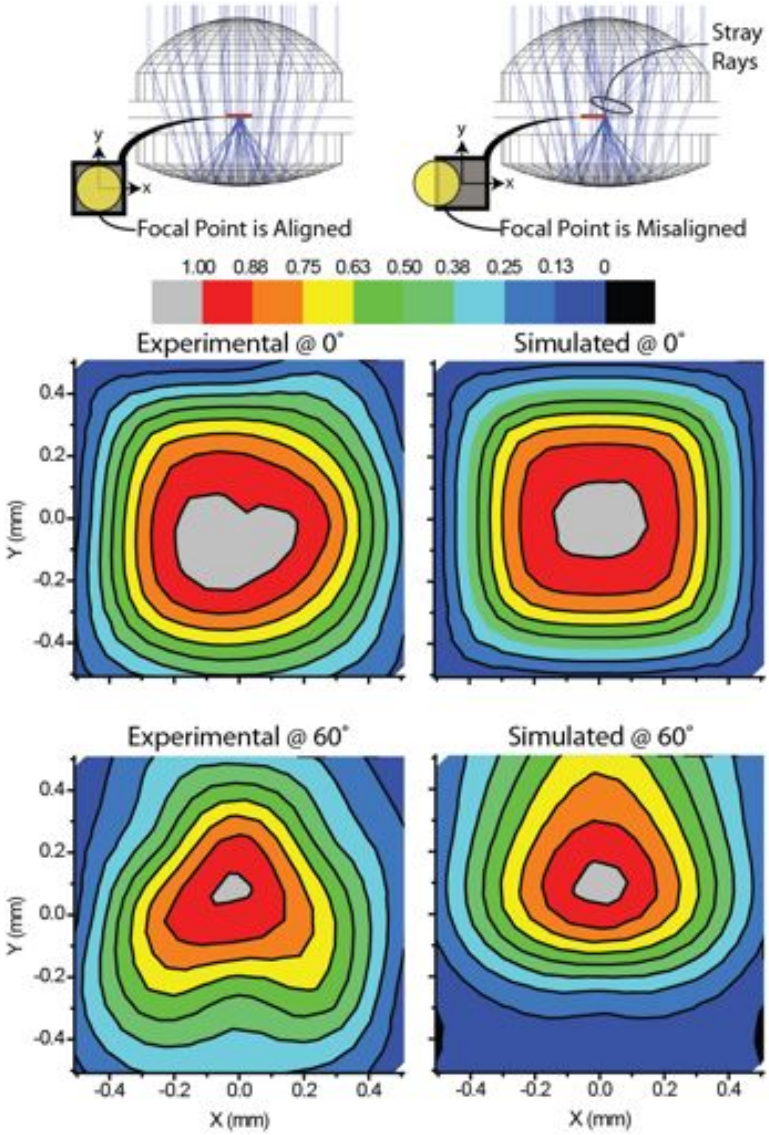

Figure 31. Experiment mapping the optical intensity profile at the microcell position by measuring the short-circuit current at varying degrees of translational misalignment. Qualitative agreement with Zemax simulation is observed in both cases.

Figure 31 explores the illumination profile and microcell positioning tolerance in more detail by mapping the photocurrent as a function of cell position relative to the focal point c.f. Figure 31a. These measurements demonstrate an alignment tolerance of approximately ±0.1 mm at normal incidence in Figure 31c that decreases to ±0.05 mm at $\boldsymbol{\theta_{inc}} = \boldsymbol{60}°$ in Figure 31e, consistent with the respective simulations in Figure 31d

and 31e. The asymmetric nature of the photocurrent map at wide angle (Figure 31e) indicates that the focal spot becomes elongated in the plane of incidence. This is due in part to the use of off-the-shelf spherical lenses and can be improved by optimizing the surface curvature with aspheric terms.

Having established that our optical model of our concentrator collection optic and scattering element are in good agreement with ray tracing simulations performed in Zemax™, we subsequently tested a complete scattering concentrator. To do this, we designed a simple 3 component system incorporating 15 mm OD off-the-shelf lenses from Edmund Optics with focal lengths of 15 mm and 40 mm for the lens and mirror, respectively, and a 1/8" thick, 1" wide acrylic bar from McMaster-Carr. A scattering element was molded into the center of the acrylic bar by heating up a custom metal biparaboloid to ~120 °C and pressing it into the acrylic surface with ~200 lb, holding it there for ~20 s, and slowly removing it. Both the mirror and the scattering element were coated with 200 nm of Ag through thermal evaporation. Finally, 6 silicon photodiodes (Newark p/n: 05M1272) were index matched to the edge of the waveguide sheet using Cargille optical gel (Cargille p/n: 081160).

The concentrator was assembled using deionized water as the low-index cladding fluid/lubricant and tested under collimated white light with angles of incidence ranging from 0° to 65°. For reference, the experimental setup is shown in Fig. 32a with a close-up of the assembled scattering concentrator in the inset. Fig. 32b depicts a close up of the waveguide pre-assembly; note that although the solar cells do not completely cover all of the exposed edge area of the waveguide, this should not greatly perturb the results of the experiment, as the majority of light gets scattered down towards either of the short edges of the waveguide.

Normalized results from the experiment and simulation (Fig. 32c) show reasonable agreement in shape, and due to the optical performance of this lens/mirror/paraboloid combination, both outperform the cosine projection intensity loss intrinsic to any static planar design for majority of the angles tested. Possible reasons for differences between the prototype and simulation include imperfections on the surface of the waveguide which would act to out couple light, large-scale surface shape deviations on the parabolic imprint, imperfect index matching/registration between the solar cells and waveguide edge, and the fact that although the solar cells cover a large fraction of the waveguide edge-area, their effective active area was unknown. These all may have contributed to reduced waveguide-PV coupling and could have had a somewhat nonlinear effect as the angle of incidence changed owing to the varying angular distribution of light within the waveguide. In addition to this test, we also placed the waveguide in an integrating sphere and performed a spectrally resolved scattering efficiency test with monochromatic light ranging from 400 nm to 1100 nm. This shows that the scattering efficiency of the paraboloid is ~constant around 88% nearly independent of wavelength which is easily understood, as mirrors do not suffer from the same chromatic aberration that a refractive system might.

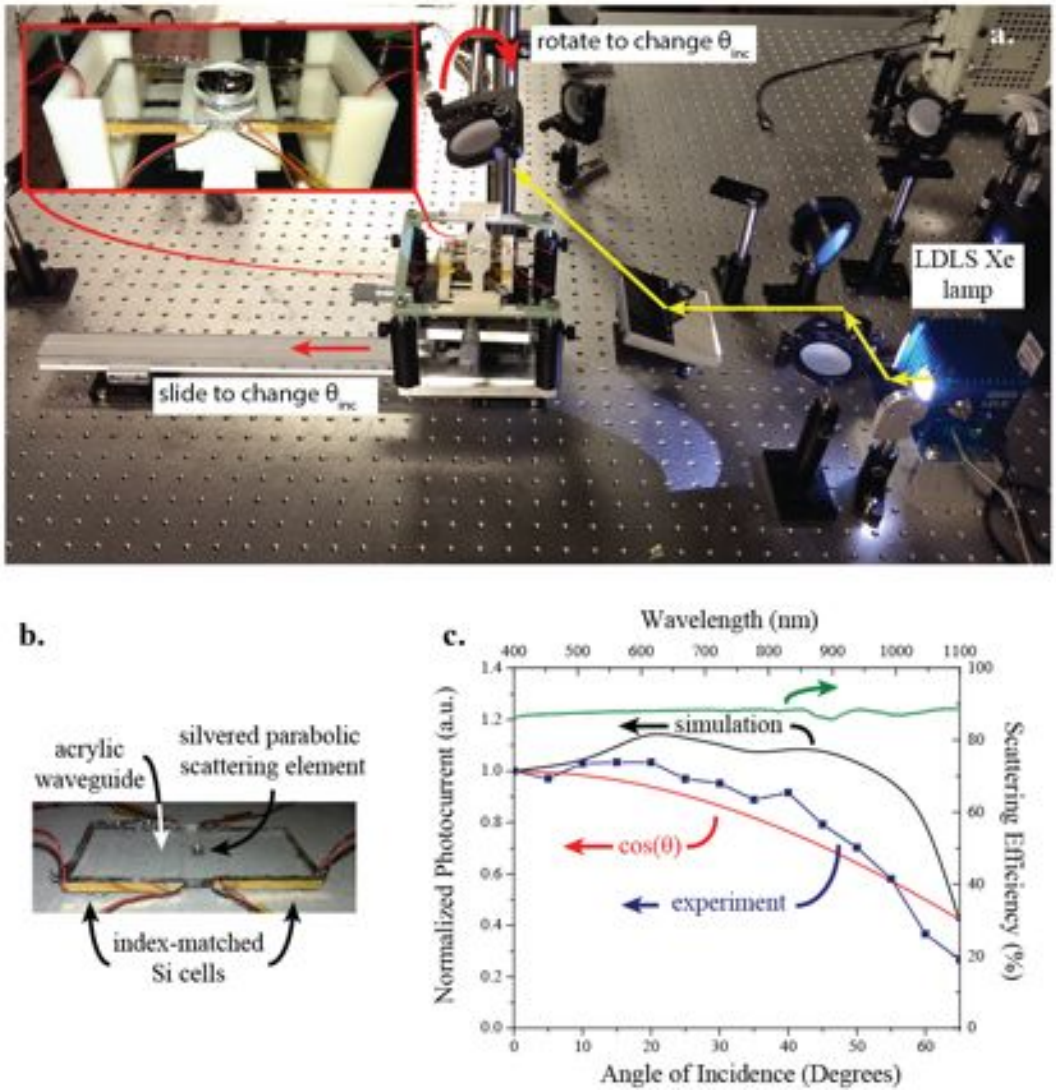

Figure 32. **(a)** The experimental test track. Broad-spectrum white light from an Energetiq laser driven light source (LDLS) was collimated and guided towards to a mirror above the concentrator; by rotating this mirror and sliding the concentrator assembly down the track as shown, the effective angle of incidence was changed. The scattering element was recoupled to the focal spot by adjusting the micrometer stages on which the concentrator sits. A close-up of the assembled concentrator is shown in the inset. **(b)** The acrylic waveguide as-tested. The Si solar cells index matched to the sides of the waveguide achieve ~90% coverage, but the majority of coupled light was guided to either the far-left or –right cells. (c) Experimental (blue), simulation (black), and cosine projection losses (red) normalized to the photocurrent at 0° as a function of angle are compared on the left axis and scattering efficiency as a function of incident wavelength is shown on the right axis.

The environmental stability of plastic lenslets and concentrator optics deployed in the field remains a continuing question. Short term data and analysis have been conducted and reviewed by Miller and Kurtz over several different publications.[7,8] In the

case of the most common CPV lens material, polymethylmethacrylate (PMMA), the dominant modes of degradation include ultraviolet-induced photodegradation (chain scission, depolymerization, which lead to yellowing and decreased ultraviolet transmission), soiling transmission loss, and mechanical failure modes (cracks, crazing, and fatigue fracture). The degree of UV-induced degradation varies widely depending on UV stabilizer additives that are proprietary to various manufacturers of PMMA. From data collected in a variety of outdoor testing locations, the typical loss in transmission relevant for CPV operation ranges 1-4% over 2-22 years. Transmission loss due to soiling varies significantly with location and climate. Typical transmission loss over the course of a year ranges 5-10% but can in certain cases range much higher. Most of the available data is fairly old (from the 1980's) and thus there is a need for more contemporary results, which is now being addressed (e.g. data will be reported from Amonix systems at the upcoming SPIE Optics & Photonics meeting in Aug. 2014).

Relative to these baselines for CPV, the key differences of the microtracking concentration approach are 1) the thickness of PMMA is approximately double that of a typical Fresnel lens and 2) the top lenslet array presents a bumpy exterior surface as opposed to the typically smooth surface of an inward-facing CPV Fresnel lens. The former difference could nominally be expected to worsen transmission loss relative to the above Fresnel benchmark data, however whether this is true remains questionable since the majority of UV is absorbed near the PMMA surface. Thus, one would not expect UV-degradation to scale linearly with PMMA thickness; data are not currently available to assess this aspect. Similarly, soiling could be expected to be worse for a bumpy lenslet surface as compared to a smooth surface, however, soil is most likely to accumulate in the crevices between lenslets, which are the least active area for solar concentration and thus this may factor may not be significant.

Thermal modeling

Two modeling methods were undertaken, with the first being a finite element analysis via COMSOL™, and the second being the Forristal model developed by the National Renewable Energy Laboratory (NREL).[9] To reduce computational loads for the former, the planar concentrator was simplified to a 2D axisymmetric model operating under laminar flow conditions; the process flow for COMSOL is shown in Fig. 33.

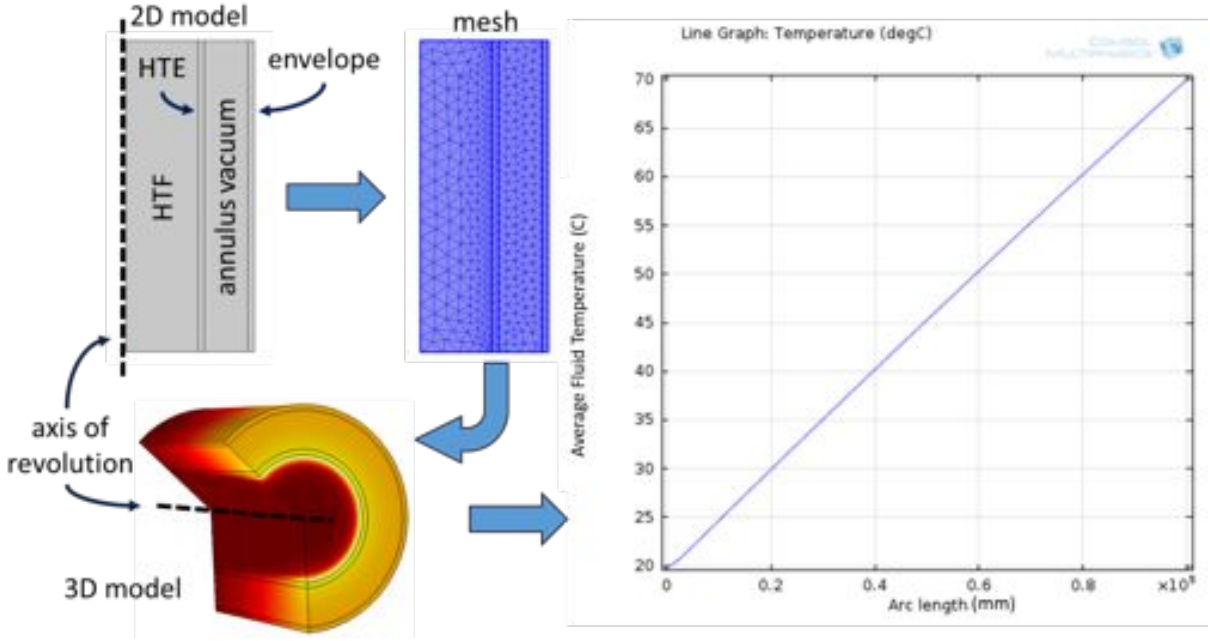

Figure 33: First, a 2D axisymmetric model containing all of the desired geometries is created. This geometry is then meshed and split into smaller sub-domains. At this point, the governing physics equations included in the model discretized and solved for each mesh element; due to the axial symmetry of this type of system, a 3D reconstruction can be performed to give additional graphics and data.

Relevant physics, such as conduction in the heat transfer element (HTE) and glass envelope walls, convection in the heat transfer fluid (HTF), low pressure air in the annulus, and air outside of the envelope, as well as uniform heat sources to simulate the solar flux were added to the model geometry. The end-fire outcoupling structure was optimized in Zemax™ to accommodate a 50 mm OD, 46 mm ID stationary linear HTE with a high coupling efficiency of 96.2%. This flux was input into COMSOL along with physics to capture radiative heat transfer rates between the HTE outer surface/glass envelope inner surface, and the glass envelope outer surface/atmosphere to complete the model.

Upon the addition of this final set of physics, the model became unsolvable at useful lengths. Iteration times required to converge to a suitably accurate solution for a 100 m length of concentrator erupted from ~5-7 min to >48 h. A set of radiation view factors must be computed for each element at a radiating surface; given a coarse mesh of ~200,000 elements, this results in a very computationally intensive solution. Although it was possible to solve ~1m lengths of the full model in a reasonable amount of time, piecing together this type of model is not amenable to the goal of comparing the planar and parabolic concentrators, as lengths of roughly 6000 m and 800 m are necessary for adequate thermal gains.

Though the first method using COMSOL™ encountered troubling computation times, the Forristal 1D and 2D models were implemented successfully. The Forristal model was initially developed to model long parabolic trough concentrators, and with minor modifications can be made to handle our planar design as well. In this model, the entire concentrator system can be characterized by four master equations given in Eqns. 1-4, which each describe heat flows per unit length within a certain region of the concentrator and will be discussed below:

$$\dot{q}'_{12conv} = \dot{q}'_{23cond} \quad (1)$$

$$\dot{q}'_{3SolAbs} = \dot{q}'_{34conv} + \dot{q}'_{34rad} + \dot{q}'_{23cond} + \dot{q}'_{cond,backet} \quad (2)$$

$$\dot{q}'_{34conv} + \dot{q}'_{34rad} = \dot{q}'_{45cond} \quad (3)$$

$$\dot{q}'_{5SolAbs} + \dot{q}'_{45cond} = \dot{q}'_{56conv} + \dot{q}'_{56rad} \quad (4)$$

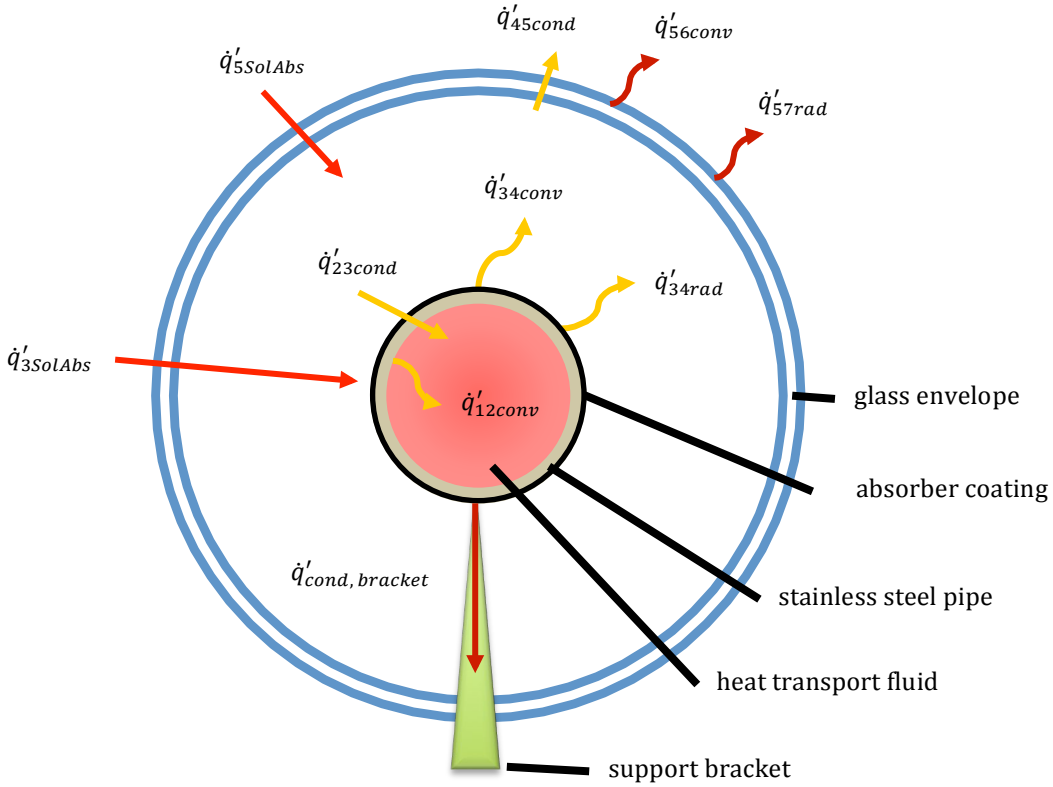

Figure 34: Forristal model of a solar concentrator. Dark red lines indicate heat loss, light red lines indicate heat gain, and yellow lines indicate heat flows internal to the system boundary

These relationships are shown schematically in Fig. 34. Equation 1 describes the convective heat transfer between HTF and the absorber the inner surface of the steel pipe, $\dot{q}'_{12conv} = h_1 D_2 \pi (T_2 - T_1)$, where h_1, D_2, T_2, and T_1 are the HTF convection heat transfer coefficient, inner diameter of the absorber pipe, inside temperature of the

pipe, and bulk temperature of HTF at the inlet, respectively. The HTF convection heat transfer coefficient is given by $h_1 = Nu_{D2}\frac{k_1}{D_2}$ with k_1 and Nu_{D2} being the thermal conductance of the HTF at T_1 and the Nusselt number based on D_2. Though we state that the analysis is to be performed in the laminar flow regime (characterized by a Reynolds number, $Re_{D2} < 2300$), the flow in this system is heavily turbulent ($Re_{D2} \approx 2E6$), owing primarily to the low viscosity of the HTF at working temperatures. As such, Nu_{D2} is given by the expression $Nu_{D2} = \frac{f_2/8(Re_{D2}-1000)Pr_1}{1+12.7\sqrt{f_2/8}(Pr_1{}^{2/3}-1)}\left(\frac{Pr_1}{Pr_2}\right)^{0.11}$, with Pr_1 and Pr_2 being the Prandlt numbers of the HTF at T_1 and T_2, respectively, and $f_2 = (1.82\log_{10}(Re_{D2}) - 1.64)^{-2}$ describing the friction factor for the inner surface of the HTE pipe. Accounting for a turbulent flow yields a heat transfer coefficient nearly one order of magnitude greater than for the turbulent case. The other side of Eq. 1 represents conduction from the absorber through the HTE wall, $\dot{q}'_{23cond} = 2\pi k_{23}\frac{(T_2-T_3)}{\ln(D_3/D_2)}$, where k_{23} is the average thermal conductance of the pipe and D_3 is the outer diameter of the pipe. Because the absorber coating is very thin, its contribution to the thermal conductivity of the pipe was neglected.

The second master equation expresses all of the interactions between the outside of the heat transfer element (HTE) and the annulus. It includes the first thermal generation term describing concentration onto the HTE, $\dot{q}'_{3SolAbs} = \dot{q}'_{si}\eta_{abs}\alpha_{abs}$ where $\dot{q}'_{si}$, η_{abs}, and α_{abs} specify the direct normal insolation (DNI) per unit length, optical efficiency of the system in delivering concentrated light to the HTE, and the absorbance of the HTE absorber film. Convection in the annulus is given by $\dot{q}'_{34conv} = h_{34}D_3\pi(T_3 - T_4)$ where h_{34} is the average heat transfer coefficient for the annulus gas, and T_4 is the temperature of the inside wall of the envelope. With the assumption that the annulus is filled with normal air under vacuum (<100 mTorr), the convective heat transfer coefficient reduces to that of free molecular convection such that $h_{34} = \frac{k_{std}}{\frac{D_3}{2}\ln\left(\frac{D_4}{D_3}\right)+b\lambda\left(\frac{D_3}{D_4}+1\right)}$ where k_{std} is the thermal conductivity of glass at standard atmospheric conditions and is equal to 0.0257 W/m-K, D_4 is the inner diameter of the glass envelope, b is the interaction coefficient of the gas which for air under 100 mTorr pressure is 1.5711, and finally, the mean free path between collisions, $\lambda = 6.6E(-12)T_{34} + 1.80E(-9)$ m. Next, conduction loss as a result of the periodic brackets that support the HTE is given by

$$\dot{q}'_{cond,bracket} = \sqrt{\overline{h_b}P_b k_b A_{cs,b}}(T_{base} - T_6)/L_{HCE},$$

where $\overline{h_b}$, P_b, k_b, $A_{cs,b}$, T_{base}, T_6, and L_{HCE} are the average heat transfer coefficient of the bracket, perimeter of the bracket, thermal conductivity of the bracket, cross sectional area of the bracket, temperature at the base of the bracket, ambient temperature, and length of the HTE, respectively. The brackets supporting the HTE were modelled as infinite fins, with the base temperature, T_{base} being 10 K less than the outside of the pipe, T_3. Finally, $\dot{q}'_{34rad} = \frac{\sigma\pi D_3(T_3^4-T_4^4)}{(\frac{1}{\varepsilon_3}+(1-\varepsilon_4)D_3/(\varepsilon_4 D_4))}$ defines the radiation between the outside of the HTE and the inside of the glass envelope where σ, ε_3, and ε_4 are the Stefan-

Boltzmann constant, the inner temperature of the glass envelope, the emissivity of the HTE absorber, the emissivity of the glass envelope, and the inner diameter of the glass envelope. Aside from the amount of incident radiation received by the absorber, the main difference between our planar design and a conventional parabolic trough is that the inner envelope surface of a parabolic concentrator is bare, leading to an ε_4 at a constant value of 0.86, whereas the inside of the envelope in the planar design is coated with ~150 nm of Ag, resulting in a significantly lower emissivity of 0.02. This potentially enables us to forgo the expensive high absorptivity, low emissivity cermet HTE coatings traditionally used in solar thermal concentrators that are required to mitigate radiation losses at high temperatures.

Master Eq. 3 expresses the interaction of the glass envelope with the air in the annulus. The only new equation here is that which details conduction through the envelope wall, $\dot{q}'_{45cond} = 2\pi k_{45} \frac{(T_4 - T_5)}{\ln(D_5/D_4)}$, where k_{45} is the average thermal conductance of the envelope and D_5 is the outer diameter of the envelope. This equation is nearly identical to the one describing heat conduction through the HTE wall to the HTF except that k_{45} was assumed to be a constant value of 1.04 W/m-K; as with the HTE absorber coating, thermal conductivity from the silver coating was ignored.

The final master equation contains the remaining heat generation and loss terms. The glass envelope absorbs some energy, as shown by $\dot{q}'_{5SolAbs} = \dot{q}'_{si}\eta_{env}\alpha_{env}$, with η_{env} being the optical efficiency of the concentrator at the glass envelope, and α_{env} being the absorptivity of the glass envelope. Convection with the ambient was modelled as $\dot{q}'_{56conv} = h_{56}\pi D_5(T_5 - T_6)$ where the convection heat transfer coefficient, $h_{56} = \frac{k_{56}}{D_5} Nu_{D5}$ with k_{56} as the thermal conductivity of air at $\frac{T_5 - T_6}{2}$ and Nu_{D5} as the Nusselt number of air convecting over the glass envelope. It was assumed there was no wind in the ambient environment, so that natural convection takes place in which case $Nu_{D5} = \left(0.60 + \frac{0.387 {Ra_{D5}}^{1/6}}{\left(1 + \left(\frac{0.559}{Pr_{56}}\right)^{9/16}\right)^{8/27}} \right)^2$ where Pr_{56} is the Prandlt number for air at the average temperature between ambient and the surface of the envelope. The Rayleigh number for air based on the outer diameter of the glass envelope, $Ra_{D5} = \frac{2g\beta(T_5 - T_6)D_5^3}{(\alpha_{56}\nu_{56})}$, with $g, \beta, \alpha_{56}, \text{ and } \nu_{56}$ are the gravitational constant of 9.81 m/s^2, the volumetric thermal expansion coefficient for an ideal gas given by $\beta = 1/T_{56}$ and the average thermal diffusivity and kinematic viscosity of air at $\frac{(T_5 + T_6)}{2}$. The last equation is used to define radiation from the glass envelope to the sky and is given by $\dot{q}'_{57rad} = \sigma\pi\varepsilon_5 D_5(T_5^4 - T_7^4)$. For both a parabolic trough concentrator and our planar microtracker, the emissivity of the outer surface of the glass envelope, $\varepsilon_5 = 0.86$, which is just that of pyrex glass. It was also assumed that the temperature of the sky was 8 K less than ambient (i.e. $T_6 - 8\,K$).

The system was constrained by setting the inlet fluid temperature, T_1, to an arbitrary value, and fluid temperature at the outlet was determined through an energy balance, $0 \approx q''_{tot}A_{tot} + \dot{m}\left[\left(h + \frac{1}{2}v^2\right)_{in} - \left(h + \frac{1}{2}v^2\right)_{out}\right]$, where q''_{tot} is the net flux per unit area, A_{tot} is the total area of the concentrator, $\dot{m}$ is the mass flow rate of the HTF, h is the enthalpy of the HTF, and v is the velocity of the HTF. Because the HTF is being heated, it will gain energy as it progresses down the tube (enthalpy will increase). At the same time, its density will decrease, and to maintain continuity of $\dot{m}$, the fluid velocity will rise.

For long receiver lengths, these latter two effects are not negligible, and can result in a miscalculation of heat loss by up to 10%; this is one of the major shortcomings of a 1D model. Now, while the Forristal model is intrinsically 1D, it can be made into a quasi-2D model by linking the inputs and outputs of adjacent 1D sections, and with an appropriate number of sections for a given length, ΔL, miscalculations of heat loss and heat gain are minimized. By using this method, and making appropriate substitutions, the outlet temperature for the i^{th} section of the concentrator can be solved for, as given by the equation below:

$$T_{out,i} = \frac{\left(\dot{q}'_{3SolAbs,i} + \dot{q}'_{5SolAbs,i} - \dot{q}'_{56conv,i} - \dot{q}'_{57rad,i}\right)\Delta L - \dot{q}'_{cond,brack,tot,i}}{\dot{m}c_{ave,i}} + \frac{\frac{1}{2}\left(v^2_{in,i} - v^2_{out,i}\right)}{c_{ave,i}} + T_{in,i}$$

where $c_{ave,i}$ is the specific heat of the HTF at the averaged temperature for that segment. With all of the necessary equations in place, we were able to solve for the final outlet temperature of the HTF for a given inlet temperature and concentrator geometry.

While parabolic troughs now utilize aperture widths on the order of 5 m, the planar concentrator is limited to a considerably smaller width to maintain a reasonable optical efficiency, as shown in Fig. 35a. To minimize power absorbed in the glass waveguide, and excessive parasitic decoupling from other scattering elements, the aperture width was limited to ~0.5 m. In this configuration, if shading error, tracking error and manufacturing imperfections are ignored, and both receiver areas are assumed to be free of dirt, the planar design still has a substantially lower optical efficiency, as seen in Fig. 35b. For reference, a full unit cell of the planar concentrator is shown in Fig. 35c.

The combination of decreased aperture size and lower optical efficiency necessitate a much longer HTE to achieve the same thermal gain. For the simulations, a typical day (March 20, 2014) in State College, PA was chosen, and the direct normal irradiance (DNI) component of the solar insolation was adjusted with an air mass correction to account for intensity changes throughout the day resulting from variation in optical path length through the atmosphere.

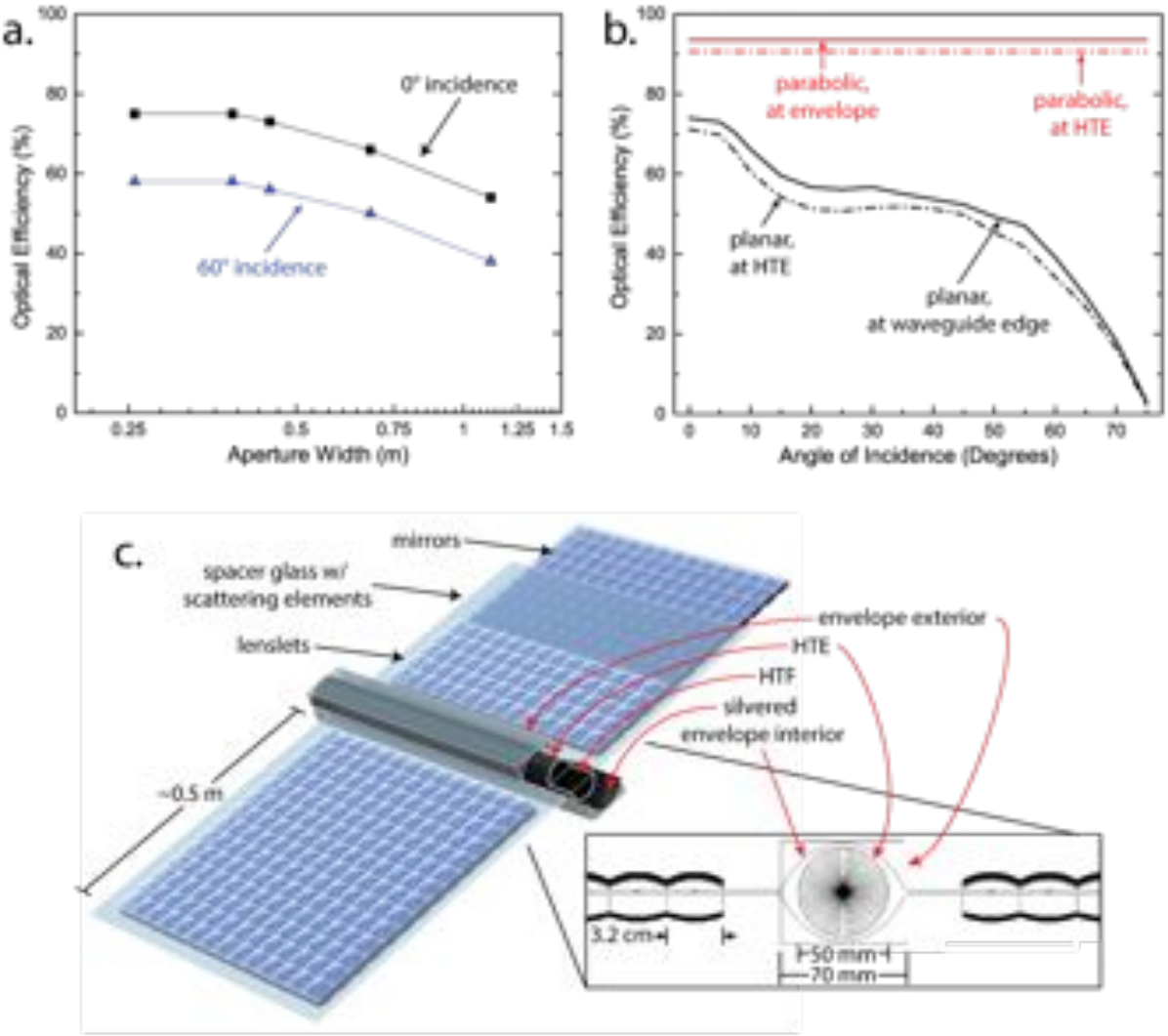

Figure 35: A comparison of the optical efficiency between a 0.5 m wide planar concentrator and 4.8 m wide parabolic concentrator (based off of the SEGS LS-2 design) assuming ideal conditions and ignoring any difference in absorption at the HTE surface as a result of different coatings.

The optimized volumetric flow rate determined by R. Forristal of 150 gpm was chosen for the parabolic trough concentrator; this flow rate was scaled to ~73 gpm for the planar concentrator to match flow inlet velocities. The length of the parabolic concentrator was ~780 m, and the length of the planar concentrator was increased 5700 m to achieve an equivalent thermal gain. A low cost black chrome coating was used for the HTE of the planar concentrator, and a traditional Luz cermet coating was used for the HTE of the parabolic concentrator.

The inlet temperature for both designs was set at 150 °C. The resulting outlet temperature as a function of time of day for both designs can be seen in Fig. 36.

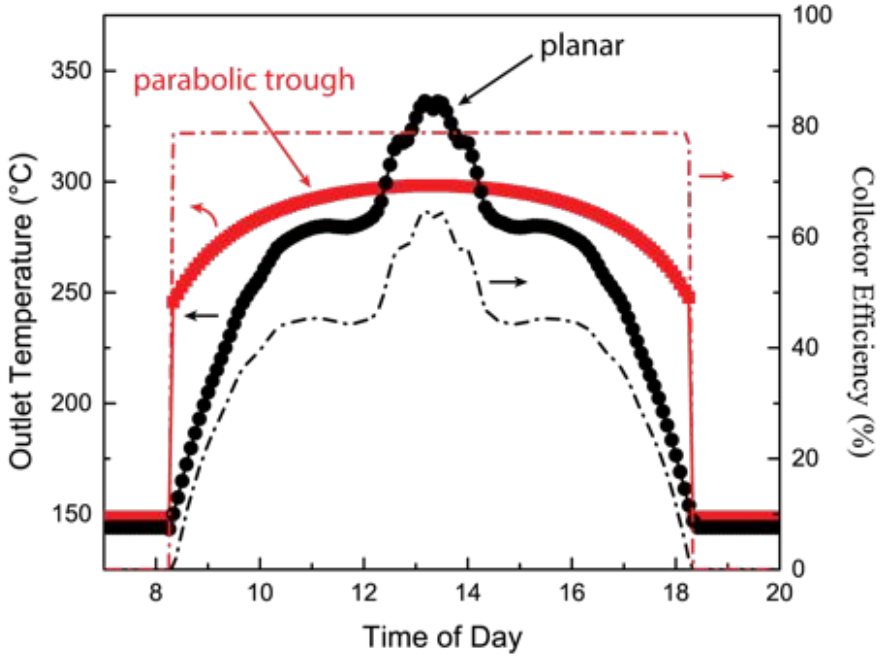

Figure 36: Outlet temperature and collector efficiency vs time of day for a 4.82 x 779.5 m^2 parabolic trough concentrator and a 0.5 x 5700 m^2 planar concentrator. Collector efficiency is defined as the ratio of collected heat in the HTF to the total incident power per aperture area, $\frac{\ddot{q}'_{12conv}}{\ddot{q}'_{inc}}$.

Because the parabolic concentrator was assumed to have perfect tracking out to 75° of incidence, its heat gain is purely dependent on the incident spectrum. It is important to note that although the planar concentrator reaches a higher absolute outlet temperature, it requires just over 7x the total length of the parabolic design to do so. When one considers the total aperture area, it may appear as though the planar design outperforms the parabolic trough in terms of per unit area (2850 m^2 vs 3760 m^2), however, due to the fact that the flow rate through the planar concentrator is roughly half that of the parabolic design, it is delivering half of the total heat, which makes it far less attractive for this type of application.

Based on these simulations, the planar microtracking design severely underperforms the parabolic trough. Although some features of the microtracking approach could be optimized, the fundamental obstacle preventing this approach from competing with the parabolic trough state-of-the-art is the much smaller aperture width and the lower optical efficiency. This combination leads to an approximate order of magnitude reduction in the solar flux delivered per unit length of the HTE and thus a corresponding increase in HTE length to compensate in order to maintain the same outlet fluid temperature.

Given that the smaller scale of scattering solar thermal concentration makes it uncompetitive with parabolic trough technology for utility-scale power generation, we subsequently investigated how the planar design performs in smaller scale settings: providing small amounts of heat to offset energy required to heat water for household uses, and a slightly larger system used to provide supplemental heating to an average household in the winter.

A typical indirect circulation system the first warms a HTF by pumping it through a flat plate concentrator similar to the one depicted in Fig. 37a and then uses a heat exchanger to transfer any thermal gain from the HTF to a standby tank to be used as hot water within the home. The use of a HTF rather than cycling water directly through the concentrator helps to mitigate any sort of issues that one might have with pipes external to the house freezing and bursting during the colder months of the year Which means that the system is applicable to a wider range of climate zones. A flat plate indirect solar water heater was chosen because it is most analogous to how our design might work, and therefore was the most direct comparison. For reference an optimized microconcentrator array is shown in Fig. 37b; this is the same design discussed in our last report with 3.2 cm wide square lenslets and a total width of 0.5m for one half unit cell.

Taking an average split level house with a total floor area of 2500 ft^2 and a southward-facing roof pitch of ~18° (this is a standard pitch of 4/12), we find that there is a total available area of ~26 m^2 to field panels for heating or collection. If we take an active solar heater/concentrator area of 4 m^2, and make the assumption that we want to raise the water tank temperature from 20 °C to 50 °C (~90 °F increase) and that we have an ideal heat exchanger such that all of the extra heat gained from the concentrator is transferred into the water tank (i.e. HTF temperature at the inlet of the concentrator will be $T_{fluid,inlet} = 50\,°\mathrm{C}$), we can find the instantaneous heating rate, P, delivered through Eq. 2,

$$P = \dot{V}\left(T_{fluid,outlet} - T_{fluid,inlet}\right)c_p\rho \qquad (2)$$

where $\dot{V}$ is the volumetric flow rate of the HTF through the concentrator, c_p is the specific heat capacity of the HTF, and ρ is the density of the HTF. For the microconcentrator, the outlet fluid temperature, $T_{fluid,outlet}$, was found as a function of time-of-day and flow rate using the modified Forristall model from the last report.

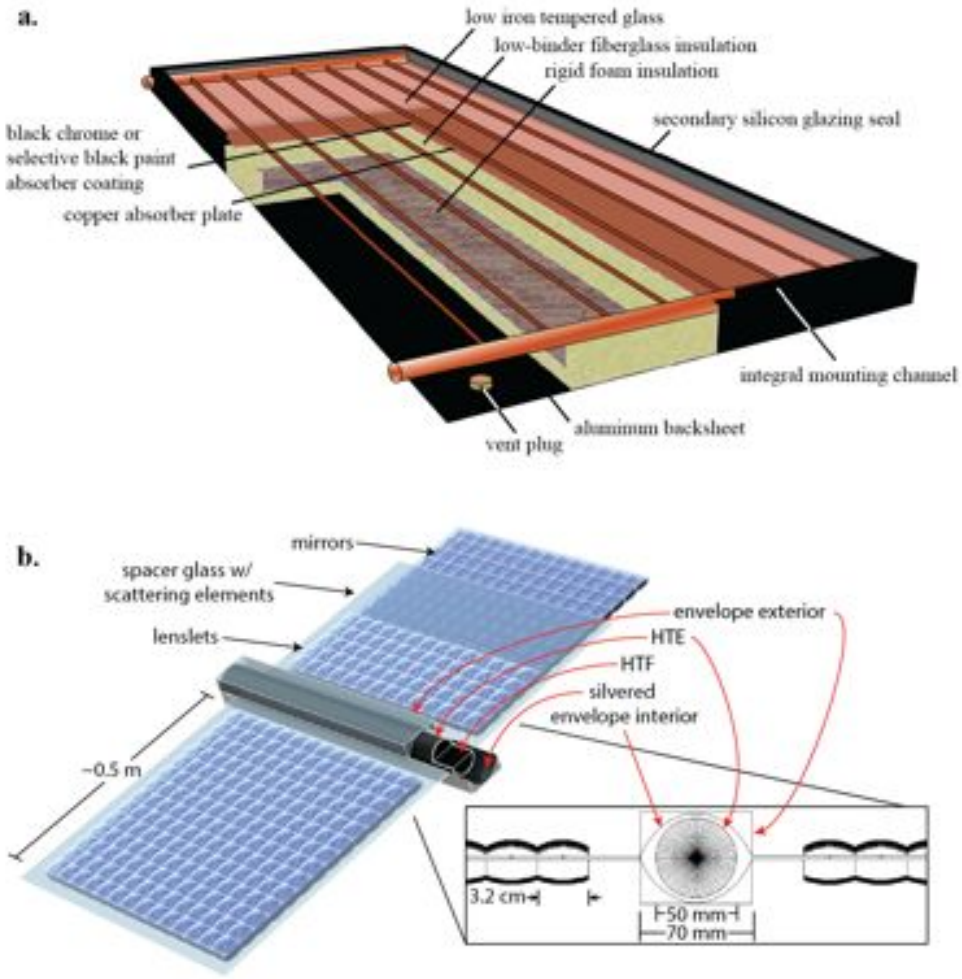

Figure 37. (a) A typical flat plate solar water heater. All internal components are sealed in an insulated box topped by a glazing that acts to protect them from weathering and ambient temperature fluctuations. Solar radiation passes through this glazing and is absorbed by a dark material which transfers a large fraction of this absorbed energy to a HTF. Image courtesy of Rheem® Solar Solutions. **(b)** One unit cell of a planar microtracking concentrator with a waveguide sandwiched between a matched lenslet/mirror combination. Given that scattering elements are manufactured directly into the waveguide, the total aperture width was limited to 0.5m to reduce parasitic decoupling and waveguide absorption. A 50mm OD HTE placed in an evacuated silvered cavity at the edge of the waveguide absorbs ~96% of the confined light.

Fig. 38 shows results that might be attained by our concentrator on a cloud-free day of March 20, 2014 with an ambient temperature of 20 °C. By integrating the instantaneous heat flow simulated at each 5 minute time step, we attained a net sum of energy captured and transferred to the water tank for an entire day of operation. Depending on the difference between the HTF inlet and ambient temperatures, ΔT, the performance of the microconcentrator is either slightly worse (~1% at $\dot{V} = 5$ gpm vs $\Delta T = 9$ °F), or significantly better (~16% at $\dot{V} = 5$ gpm vs $\Delta T = 90$ °F) than the flat plate solar collector.

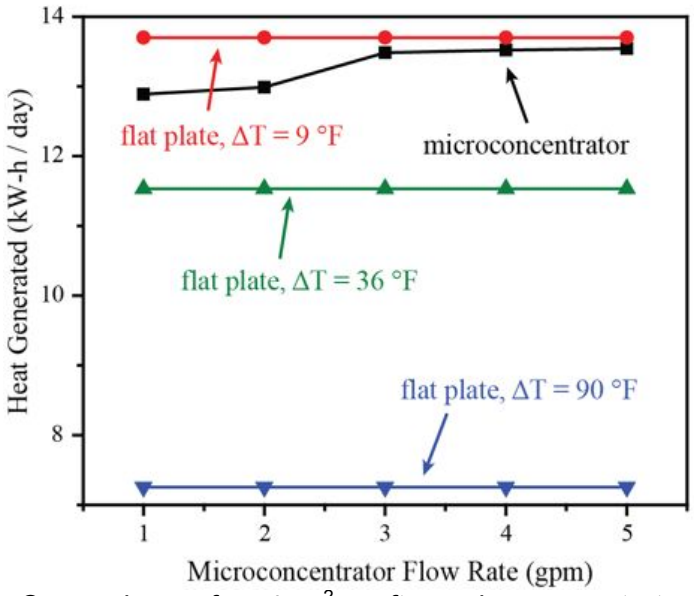

Figure 38. Comparison of a 4 m^2 rooftop microconcentrator to a flat plate collector to be used as a solar water heater in State College, PA on March 22, 2014. The flat plate design in this case is based off of a Rheem® solar collector operating at a flow rate of 1 gpm.

Knowing that we are aiming to achieve temperature differentials ≥ 90 °F, we should expect superior year-round performance from the microconcentrator. Additionally, because the HTE of the microconcentrator is under vacuum and surrounded by a low emissivity chamber, it is much more tolerant to seasonal variations in temperature. It may be of merit to note that since the rate of conductive/convective heat transfer between two bodies is proportional to the temperature difference between them, it could be desirable to operate at lower flow rates. Peak outlet fluid temperatures for the microconcentrator ranged from 53 °C to 66 °C at flow rates of 5 gpm and 1 gpm, respectively. Higher temperature differentials will result in less surface area required for a good heat exchanger, and lower flow rates will decrease the size of the pump required to move the HTF; both of these serve to reduce the cost of the system.

Another similar application would be to use the concentrator to provide auxiliary radiative heating for a home during the winter months. Depending on its age and level of insulation, a 2500 ft^2 dwelling in Pennsylvania requires ~29-32 kW (100,000 – 112,500 BTUs) to heat the house during the winter, and if we were to utilize ~100% of the available roof space, the microconcentrator should be able to contribute a sizeable portion of the power. Fig. 39 shows the heat output and collector efficiency vs time of day for Dec 22, 2014; because the sun is at its most extreme azimuth angle of the year, this is expected to be the absolute worst that the microtracking system would perform, and the same assumption of having $T_{fluid,inlet}$ being a maintained at 50 °C applies here as well. Nevertheless, this system could supply ~1/3 of the total heat required during midday.

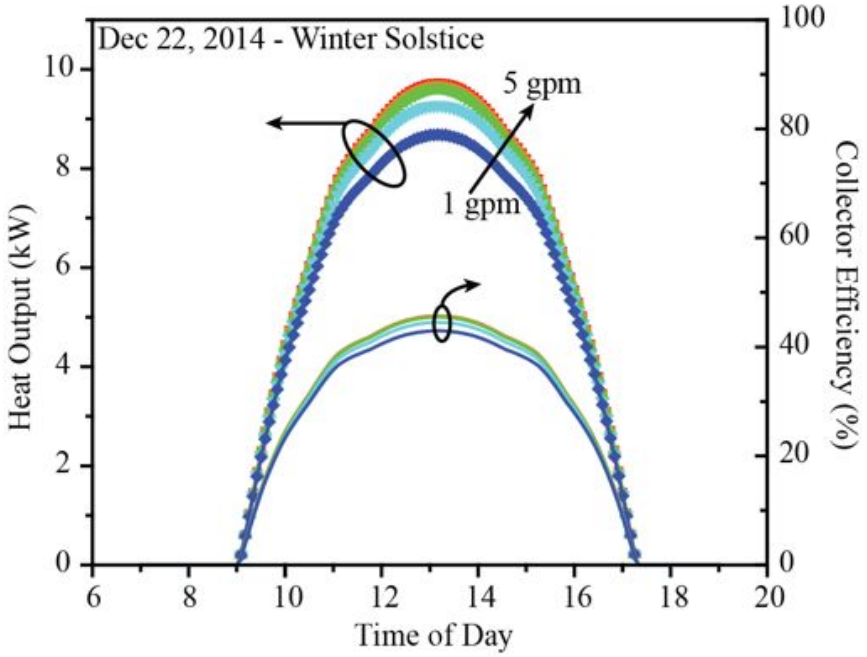

Figure 39. Heat generated by rooftop microconcentrator vs time of day on December 22, 2014, the winter solstice. Increasing flow rates leads to less loss therefore, higher heat outputs.

We could accomplish slightly higher heat gains at the cost of absolute temperature by lowering $T_{fluid,inlet}$, therefore extracting more heat from the HTF. Because the concentrator system was simulated to be tilted at the same angle as the rooftop rather than a more ideal latitude tilt (~18° vs ~41°), the primary reason for poor collector efficiency is the low optical efficiency of the system. If we were to tilt the panels at latitude, we would lose ~20% of our active area, but only pick up ~4% in peak optical efficiency.

Opportunity for concentrating photovoltaics

The concentrator stack from Fig. 28 was subsequently tested outdoors on a sunny day (May 31, 2014) tilted at latitude in State College, PA, USA from 8 am to 6 pm by manually adjusting the translational alignment every 15 minutes. Figure 40a presents a photograph of the testing arrangement showing the short-circuit current measured for neighboring microcells located in and out of the concentrator stack. As shown in Fig. 40b, the concentrator operates effectively throughout the day, maintaining a short-circuit current enhancement in the range 150 – 200x from 9 am to 5 pm. This result is in reasonable qualitative agreement with the enhancement determined under laboratory testing (Fig. 30) and thus, together with open-circuit voltage and fill-factor that were similarly maintained, equates directly to the increase in power output.

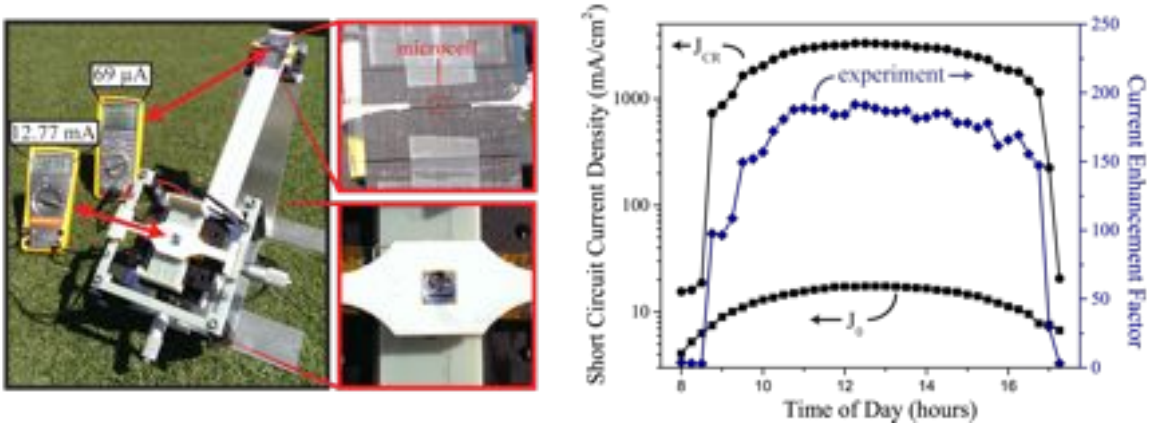

Figure 40. (a) Picture of the single cell concentrator system integrated along with a bare control cell for outdoor testing. **(b)** Short-circuit current density recorded from the bare and concentrated microcells at 15 minute intervals throughout the day on May 31, 2014 in State College, PA, USA; the right-hand axis displays the current enhancement factor.

Figure 41 shows the result for a small-scale, 7-element hexagonal lenslet array on acrylic plastic together with a corresponding array of GaAs microcells transfer-printed on a glass substrate. These components were assembled as shown schematically in Figure 41a to yield a full concentrator stack approximately 1 cm thick with each series-connected row of microcells contacted independently. Figure 41b displays the ratio of net short-circuit current measured in and out of the concentrator stack along with that predicted by ray tracing simulation. Here, we observe a peak current enhancement ratio of ~150 that is substantially lower than predicted for the design target.

This difference is similar to that measured for a single cell from the array, indicating that surface error in the printed lenslets (as opposed to misalignment of the microcell array positions) is the main factor leading to subpar performance. Although precision interferometry was not available to rigorously characterize the lenslet surfaces, profilometry of a small section of printed lenslet along with the aberration induced in a Gaussian beam and a comparison of simulated concentrator performance (red line) all suggest that relatively large scale surface error (~20%) is mainly responsible for the lower-than-expected performance.

Despite the lenslet fabrication error, which could be improved by refining the printoptical process or using molded optics, the initial result in Fig. 41b demonstrates that the requisite microcell patterning and alignment can be achieved, validating the notion of a larger scale microtracking microcell CPV array. To this point, Fig. 41c presents outdoor testing results for the prototype array conducted in State College, PA, USA on June 1, 2014, where the concentrator maintains a current enhancement ratio in the range 100 – 150x relative to the bare reference cell for over six hours.

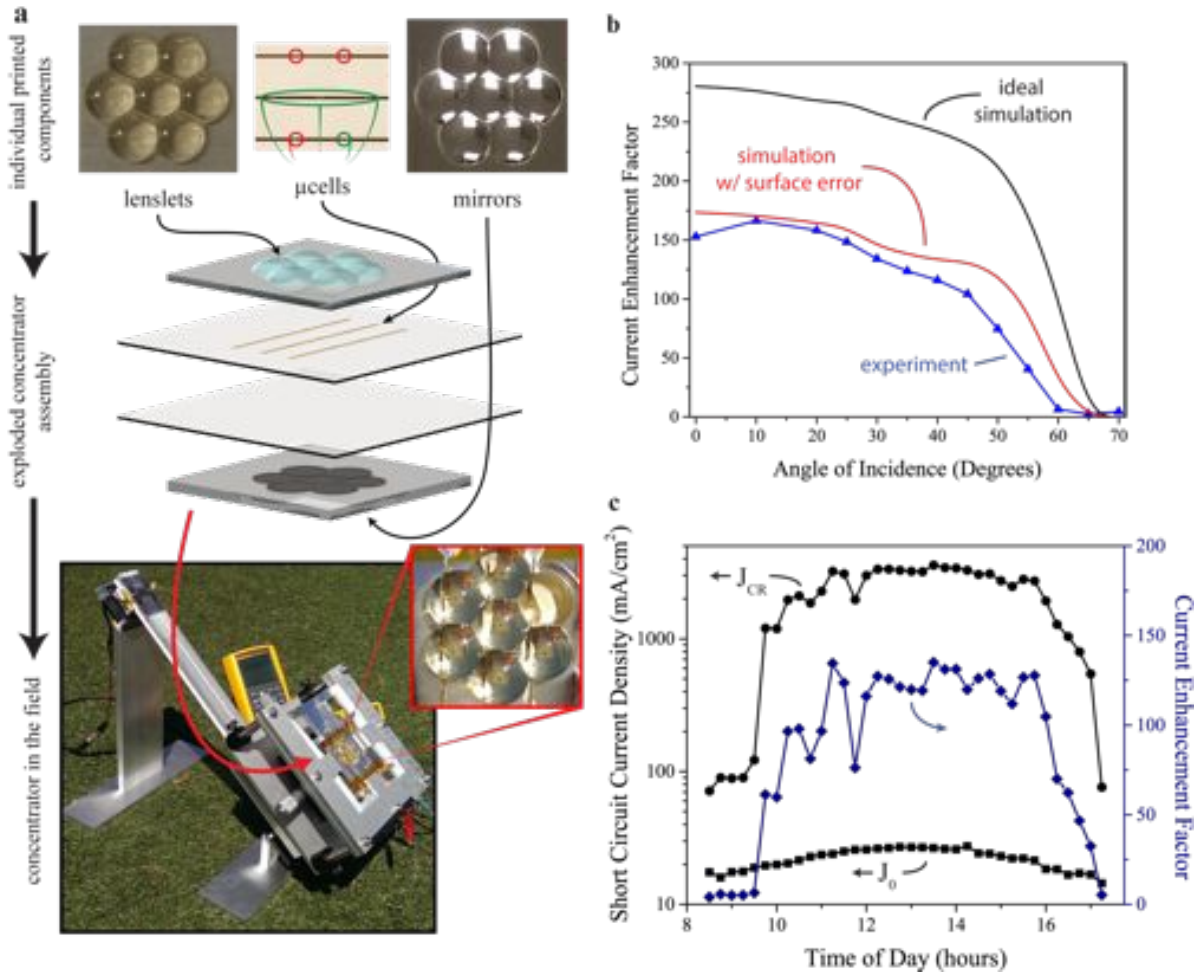

Figure 41. **(a)** Photographs showing the refractive top and reflective bottom 3D-printed lenslet arrays together with the corresponding layout of GaAs microcells used to construct the concentrator prototype. These components were assembled as illustrated in the diagram to create the full concentrator stack shown in photographs of the outdoor testing configuration at bottom. The cells circled in red (top) were damaged during assembly and excluded (by shorting across them) from measurements; the total photocurrent is the sum of that collected from the bottom right cell and the series-connected middle row of three cells circled in green. **(b)** Ratio of the short-circuit current recorded from the concentrator stack under collimated Xe lamp illumination relative to that recorded for the bare microcell array outside the concentrator. The measured photocurrent gain is substantially lower than that predicted for this design via ray tracing simulation (solid black line) due to surface error in the printed lenslets. Qualitative agreement is obtained by incorporating Gaussian surface scatter and curvature error into the ray tracing simulation (red line) to model the impact of fabrication defects. **(c)** Short-circuit current recorded from the prototype array and from the bare reference under full day outdoor testing as shown in (a); the current enhancement ratio is indicated on the right-hand axis.

Cosine projection loss constitutes a fundamental concern for fixed-tilt solar concentration. Whereas polar tracking maintains sunlight at normal incidence, the intensity falling on a fixed panel decreases as the cosine of the incidence angle and

thus, per unit panel area, a fixed-tilt system is inherently less efficient than a polar tracking system. This difference is quantified in Fig. 42b, which compares the hourly power output per unit panel area at the vernal equinox in State College, PA, USA for an optimized microtracking panel with a conventional Fresnel lens at equivalent 255x geometric gain assuming a solar cell efficiency of 30%. Integrated over the day, the polar tracking CPV system delivers approximately 1.5x more energy than the fixed-tilt microtracking system, typical of the difference throughout an entire year.

By the same measure however, polar tracking panels must be spaced farther apart to avoid shading one another as illustrated in Fig. 42a and thus cosine projection loss is offset when power generation per unit installed land area is the relevant metric. Because microtracking panels can be spaced closely in the east-west direction without shading one another, more power generating capability can be located in a given area of real estate than for polar tracking systems. As shown in Fig. 42c, microtracking PV consequently delivers more power per unit land area over the majority of a typical day, resulting in an approximate 1.9x increase in energy output. Compared with an equivalent installation of Si photovoltaics assuming a module efficiency of 18% (gray line), we project a 30% increase in daily energy output delivered by the microcell CPV system.

As compared to traditional Fresnel lens CPV systems, embedded microcell microtracking may hold several advantages, particularly for enabling CPV application in urban areas and on rooftops where orientation-based systems have so far been impractical. In addition to improved land use efficienc, microtracking is expected to reduce susceptibility to wind load tracking error and simplify the overall support and tracking infrastructure. At approximately 1 cm thick, microtracking concentration is mechanically simpler and far more compact than previous approaches to fixed panel CPV, with substantially higher optical efficiency owing to the index-matched nature of the concentrator stack. Because lateral displacement of the microcell sheet is limited to ~1 cm (i.e. the lenslet pitch) and all movement interfaces are internal and protected, this approach should be mechanically robust, in many respects resembling fixed-panel PV more than traditional CPV.

Cost and scalability are also addressed. High efficiency microcells are now fabricated economically in releasable, multilayer stacks and transfer-printing has been demonstrated to pattern and connect them with sub-micron precision and high yield over large (Gen 2.5) areas. Recent cost analysis and commercial success for microcell CPV systems support the potential of this manufacturing approach to be cost-competitive in the photovoltaic marketplace. Simple modes of automated translational microtracking have already been demonstrated[1] and injection molding enables low cost, high throughput fabrication of plastic lenslet arrays using the same stabilizer additives as existing CPV Fresnel lenses to mitigate ultraviolet-induced yellowing. Long-term color stability is also documented for index-matching fluids under solar illumination. Mechanical weathering and soiling of the upper lenslet surface are an inevitable concern with plastic optics, though major surface damage could ultimately be resolved by sliding off and replacing the upper lenslet array.

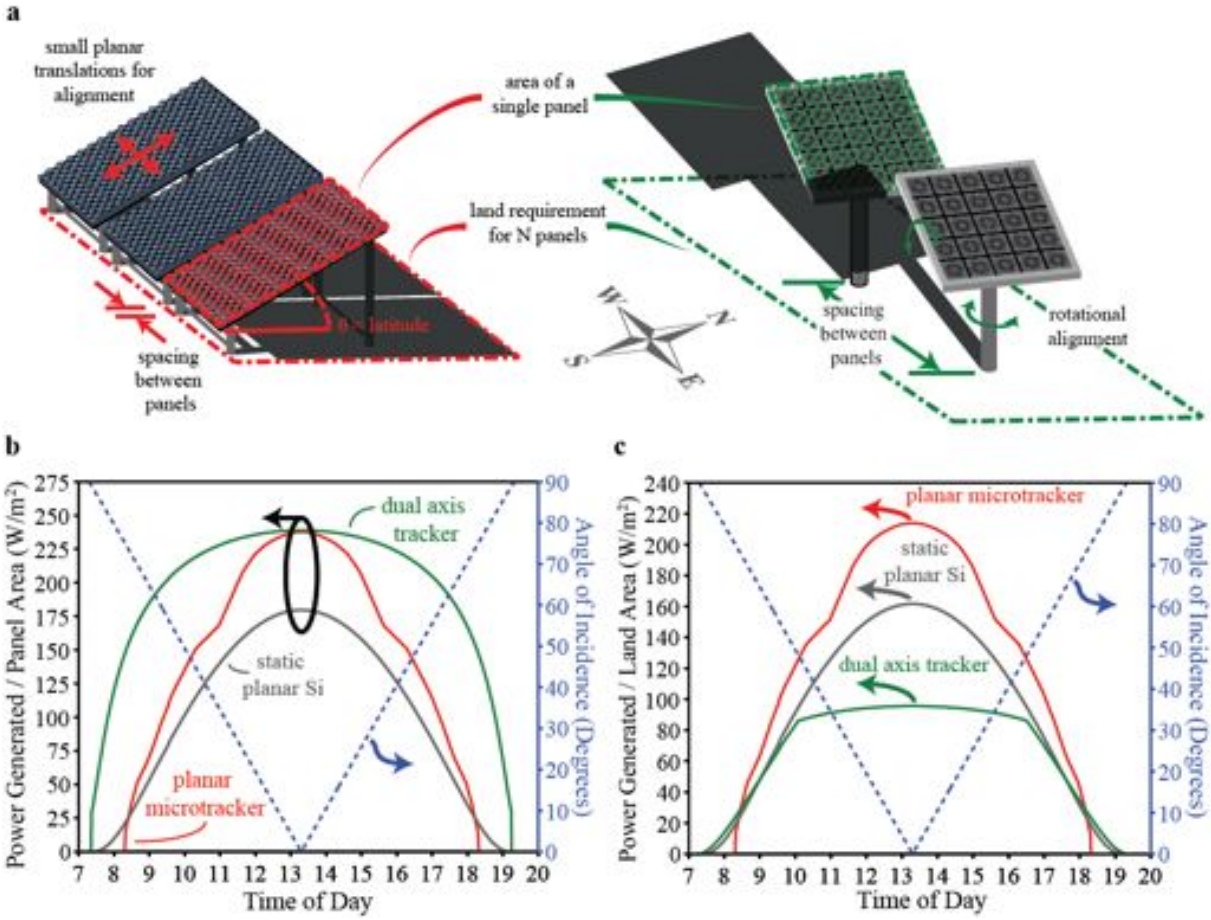

Figure 42. (a) Physical layout of an east-west oriented line of latitude-tilted microtracking panels spaced adjacent to one another. Dual axis tracking conventional Fresnel-based CPV panels shown for comparison must be spaced farther apart to avoid shading one another. **(b)** Simulated power generation per unit panel area for the microtracking and dual axis systems in (a) along with a latitude-tilted Si photovoltaic module for comparison (gray line). The spacing between dual axis panels is unconstrained and large enough to entirely avoid shading. The dashed line (right-hand axis) designates the solar incidence angle for the fixed-tilt microtracking panels. **(c)** Power generated per unit installed land area for each system; the dual axis panel spacing in this case is optimized to avoid shading for tilt angles up to 50°. As compared to (b), in this case the planar microtracking system generates nearly twice as much energy on aggregate as the dual axis system over a typical day since more microtracking panels can be located in a given land area without shading.

While the detailed impact of thermal expansion and refractive index change arising from climatic variation remains to be investigated, initial estimates suggest a negligible change in focal length and spot size over a 50°C temperature swing whereas registration between the microcell and lenslet arrays should be maintained since both are constructed on/from the same plastic.

Taken together, our results demonstrate microcell microtracking as a viable route to combine the high efficiency and cost leverage of CPV with the siting versatility and operational robustness of fixed panel PV. Anti-reflection coatings applied to the upper lenslet and microcell surfaces are predicted to maintain full-day optical efficiency between 80% and 95% whereas additional optimization of the lenslet surfaces and microcell size should further increase the concentration ratio. Supported by the development of multijunction tandem microcells with demonstrated efficiency exceeding 40%,[10] the embedded microtracking approach developed through this program may provide a new path for efficient, compact, and inexpensive photovoltaic power.

Conclusions:

The results of this program demonstrate that waveguide-based scattering concentration can be efficient at small scale (<0.5 m aperture width), but that it is not scalable to larger areas owing to unavoidable parasitic waveguide out-coupling losses and material absorption. This fact was shown via thermal modeling to significantly limit the heat transfer fluid outlet temperature and flow rate that could be achieved with a given length of heat transfer element tube relative to state-of-the-art parabolic trough systems. Consequently, the finding of this work is that scattering solar thermal concentration is not viable for utility-scale CSP power generation. In contrast, this work has shown that, in application to concentrating photovoltaics, the developed concepts have the potential for transformative change by enabling high efficiency CPV systems to be sited on rooftops and in urban environments, which has not previously been possible and may open up a new CPV market opportunity.

Budget and Schedule:

Below is our budget period summary.

Budget Period 1:

Phase I budget period: 8/1/2012 – 7/31/2013

Phase I DOE share: $96,403

Phase I Cost share: $24,100

Budget Period 2:*

Phase II budget period: 8/1/2013 – 12/31/2014**

Phase II DOE share: $63,108

Phase II Cost share: $15,777

*The original 3-year program was revised to two years following the first year continuation evaluation.

**A no-cost extension was granted at the nominal end of the program (10/31/2014) in order to enable the budget portion allocated for student tuition support to be fully spent out through the conclusion of the fall 2014 semester.

Path Forward:

Waveguide-based scattering concentration was shown in this program not to be viable at utility scale for CSP power generation, and so should not be pursued further. By contrast, microtracking microcell CPV benefits uniquely from the optical designs created through this work and holds real commercial potential. This concept will thus continue to be pursued, with the goal of moving beyond the proof-of-concept stage achieved though this program and creating a larger scale prototype panel in collaboration with academic and industry partners that will push the performance of this technology and evaluate costs and manufacturing potential.

A patent disclosure was submitted to the Penn State Tech Transfer office on April 11, 2014 for the CPV technology developed through this program, but PSU decided not to pursue a full patent application because the core concepts had already been publicly disclosed more than a year prior (thereby eliminating international rights) in slides posted on the SunShot website following the 2013 SunShot Review meeting. The CPV work was published in Nature Communications in Feb. 2015:

- J.S. Price, X. Sheng, B. Meulblok, J.A. Rogers and N. C. Giebink, “Wide-angle microtracking for quasi-static microcell concentrating photovoltaics”, *Nat. Commun.* **6**, 6223 (2015) DOI: 10.1038/ncomms7223

References:

1 Hallas, J. M., Baker, K. A., Karp, J. H., Tremblay, E. J. & Ford, J. E. Two-axis solar tracking accomplished through small lateral translations. *Appl. Optics* **51**, 6117, (2012).

2 Baker, K. A., Karp, J. H., Tremblay, E. J., Hallas, J. M. & Ford, J. E. Reactive self-tracking solar concentrators: concept, design, and initial materials characterization. *Appl. Optics* **51**, 1086, (2012).

3 Tremblay, E. J., Loterie, D. & Moser, C. Thermal phase change actuator for self-tracking solar concentration. *Opt. Express* **20**, A964, (2012).

4 Zagolla, V., Tremblay, E. J. & Moser, C. Light induced fluidic waveguide coupling. *Opt. Express* **20**, A924, (2012).

5 Bowden, N., Brittain, S., Evans, A. G., Hutchinson, J. W. & Whitesides, G. M. Spontaneous formation of ordered structures in thin films of metals supported on an elastomeric polymer. *Nature* **393**, 146, (1998).

6 Koo, W. H., Jeong, S. M., Araoka, F., Ishikawa, K., Nishimura, S., Toyooka, T. & Takezoe, H. Light extraction from organic light-emitting diodes enhanced by spontaneously formed buckles. *Nat. Photon.* **4**, 222, (2010).

7 Miller, D. C., Carloni, J. D., Johnson, D. K., Pankow, J. W., Gjersing, E. L., To, B., Packard, C. E., Kennedy, C. E. & Kurtz, S. R. An investigation of the changes in poly(methyl methacrylate) specimens after exposure to ultra-violet light, heat, and humidity. *Sol. Energy Mat. Sol. Cells* **111**, 165, (2013).

8 Miller, D. C. & Kurtz, S. R. Durability of Fresnel lenses: A review specific to the concentrating photovoltaic application. *Sol. Energy Mat. Sol. Cells* **95**, 2037, (2011).

9 Forristall, R. Heat transfer analysis and modeling of a parabolic trough solar receiver implemented in engineering equation solver. (National Renewable Energy Laboratory, 2003).

10 Sheng, X., Bower, C. A., Bonafede, S., Wilson, J. W., Fisher, B., Meitl, M., Yuen, H., Wang, S., Shen, L., Banks, A. R., Corcoran, C. J., Nuzzo, R. G., Burroughs, S. & Rogers, J. A. Printing-based assembly of quadruple-junction four-terminal microscale solar cells and their use in high-efficiency modules. *Nat. Mater.* **13**, 593, (2014).